FACULDADE DE ENGENHARIA DA UNIVERSIDADE DO PORTO

Fibre recruitment of the bladder during filling

Nuno Filipe Leite Barros

Mestrado Integrado em Engenharia Mecânica

Supervisors:
Dr. João Ferreira
Prof. Dr. Marco Parente
Prof. Dr. Renato Natal

28 June, 2021

Fibre recruitment of the bladder during filling

Nuno Filipe Leite Barros

Mestrado Integrado em Engenharia Mecânica

28 June, 2021

Abstract

Bladder dysfunction affects millions of people worldwide, with a significant impact not only on their quality of life, both physically and psychologically, but also on the health-care system. Addressing the bladder through a biomechanics approach can lead to a better understanding of bladder dysfunction and identify better therapeutic interventions.

The main objective of this work is to develop a new constitutive model capable of describing the behaviour of the bladder as it is being filled. Modelling the bladder high compliance requires a new, microstructure-based material model encompassing fibre recruitment during filling and dispersion of the fibres.

Uniaxial test of a female porcine bladder were conducted experimentally during this work to characterize and define the parameters on which the proposed constitutive model is based.

The new material model was implemented in a finite element simulation of the bladder filling using a user-defined material UMAT.

Fitting of the proposed constitutive model to experimental data suggested a good characterization of the bladder wall behaviour. Conducted simulations suggested a correct implemen-tation of the material model in the UMAT, as well as the fibre recruitment and dispersion assessment.

Keywords: Bladder, Biomechanics, Fibre recruitment, Fibre dispersion, Constitutive model

Resumo

Disfunções da bexiga afetam milhões de pessoas mundialmente, com um impacto significativo não só na sua qualidade de vida, tanto a nível físico como psicológico, mas também nos sistemas de saúde. Estudar a bexiga numa vertente de biomecânica pode levar a uma melhor compressão das disfunções e identificar intervenções terapêuticas mais atrativas.

O objetivo principal deste trabalho é desenvolver um modelo constitutivo capaz de descrever o comportamento da bexiga enquanto enche.

Modelar a elevada extensibilidade da bexiga requer um novo modelo material, baseado na microestrutura da bexiga, que engloba o recrutamento das fibras durante o enchimento e a sua dispersão. Ensaios uniaxiais a uma bexiga de origem suína foram realizados experimentalmente durante o desenvolvimento deste trabalho com o intuito de caracterizar e definir os parâmetros nos quais o novo modelo constitutivo se baseia.

O novo modelo material foi implementado numa simulação por elementos finitos do enchimento da bexiga usando um material definido pelo utilizador com recurso a uma UMAT.

Ajustes do modelo constitutivo proposto a curvas experimentais sugerem uma boa caracterização do comportamento da bexiga. As simulações realizadas indicam uma correta implementação do modelo material na UMAT assim como uma correta abordagem ao recrutamento e dispersão de fibras.

Palavras-Chave: Bexiga, Biomecânica, Recrutamento de fibras, Dispersão de fibras, Modelo Constitutivo

Agradecimentos

Ao meu orientador, Doutor João Ferreira, agradeço toda a disponibilidade durante o desenvolvimento deste trabalho. Agradeço também a maneira de trabalhar, cultivando sempre o meu espirito crítico. Agradeço por fim todo o apoio, conhecimentos e amizade.

Ao Professor Doutor Marco Parente, agradeço não só a confiança em mim depositada ao longo destes últimos anos, mas também as condições de trabalho que me proporcionou e todo acompanhamento constante.

Ao Professor Doutor Renato Natal pelas dicas e conhecimentos transmitidos ao longo da realização deste trabalho.

Ao Professor Doutor João Neves Pinto, agradeço toda a amizadade e conselhos ao longo da minha formação universitária.

Ao Tiago Sabino e Francisco Teixeira, agradeço por todo o companheirismo e amizadade ao longo do curso.

À minha Família e Namorada, Renata, agradeço todo o carinho e acompanhamento.

Aos meus Irmãos, Matilde e Pedro, agradeço a amizade e companhia.

À minha Mãe e ao meu Pai, Raquel e Nuno, agradeço por tudo, e em especial por me terem permitido ser sempre a melhor versão de mim.

Obrigado, por tudo.
Nuno

"If I have seen further,
it is by standing on the shoulders of Giants."

Sir Isaac Newton

Contents

List of Figures

List of Symbols

Ω	R^3 Domain
$\mathbf{B}_0$	Reference configuration
$\mathbf{B}_t$	Current configuration
t	Time
$\mathbf{X}$	Material coordinates
$\mathbf{x}$	Spatial coordinates
φ	Motion mapping
$\mathbf{u}$	Displacement
$\mathbf{F}$	Deformation gradient
$\mathbf{I}$	Identity tensor
J	Jacobian
$\mathbf{C}$	Right Cauchy-Green deformation tensor
$\mathbf{b}$	Left Cauchy-Green deformation tensor
$\mathbf{E}$	Lagrangian strain
$\mathbf{E}$	Eulerian strain
$\mathbf{R}$	Rotation tensor
$\mathbf{U}$	Right stretch tensor
$\mathbf{V}$	Left stretch tensor
V_0	Reference volume
V_t	Current volume
S_0	Reference surface
S_t	Current surface
$\mathbf{f}$	Force
$\boldsymbol{\sigma}$	Cauchy stress tensor

$\mathbf{P}$	First Piola-Kirchhoff stress tensor
$\mathbf{S}$	Second Piola-Kirchhoff stress tensor
$\boldsymbol{\tau}$	Kirchhoff stress tensor
$\mathbb{C}^{tan}$	Tangent matrix or Material elastic tangent stiffness
Ψ	Strain-energy function
Ψ_{iso}	Isochoric part of the strain-energy function
Ψ_{vol}	Volumetric part of the strain-energy function
Ψ_{mat}	Matrix contribution of the strain-energy function
Ψ_{fib}	Fibre contribution of the strain-energy function
$I_{1,2,3}$	Invariants of the Cauchy-Green deformation tensors
$I_{4,5}$	Anisotropy pseudo-invariants of the Cauchy-Green deformation tensors
λ	Stretch
λ_{f}	Fibre Stretch
λ_{r}	Recruitment Stretch
$\mathbf{a}_0$	Unit vector at reference configuration
$\mathbf{a}$	Unit vector at current configuration
$\mathbf{N}$	Reference fibre orientation
$\mathbf{H}$	Generalized structure tensor
$\mathbb{S}^2$	Unit sphere
$\rho(\mathbf{N})$	Probability density function

Chapter 1

Introduction

1.1 Context

The bladder is a hollow and highly distensible organ with a complex structure consisting on several distinctive layers. Its main function is to store and expel urine in a controlled process, known as a micturition cycle. Alterations to this cycle, caused by a number of conditions ranging from an urinary tract infection to bladder cancer, have a significant impact on the life of patients [1, 2].

Biomechanics is the study of biological systems using mechanical concepts as force, stress, deformation, and motion. The physical properties of materials are specified by constitutive equations. Following an extensive research on the topic, there has been substantial progress in the development of constitutive models to describe the behaviour of soft biological tissues. These models can provide a helpful understanding of pathologies, offering a complementary approach to therapeutic interventions. Despite recent progression in constitutive equation model development, there is still a need to define a model capable of describing the mechanical behaviour of the bladder wall [3].

The intention of this work is to propose a new constitute model based on a pseudostrain-energy function capable of describing the bladder wall. The proposed pseudostrain-energy function is based on the microstructure of the bladder, addressing the fibre recruitment and dispersion characteristic of the bladder wall histology.

The characterization and the definition of the parameters on which the proposed model is based, is done by a phenomenological approach, where the model is fitted to experimental data from uniaxial tests conducted during this work.

In this work, it is also expected to implement the new proposed model in a numerical simulation of the bladder filling, using an existing model of a bladder obtained from magnetic resonance imaging. Consequently, it is necessary to use a user-defined material with the constitutive equations on which the proposed model is based.

1.2 Thesis Organization

Chapter 2 of this thesis provides an overview of the bladder and urinary tract. The anatomy of the bladder as well as its histology is presented. Bladder normal behaviour and the effect of clinical conditions are regarded. Furthermore, the role of biomechanics is discussed.

Chapter 3 provides an overview of the fundamental concepts of continuum mechanics. Kinematics variables, common strain and stress measures are defined. Material response to deformation and volume change is address. Finally, the fibre spatial orientation is discussed.

Chapter 4 describes the bladder mechanical behaviour and presents some strain-energy functions. The proposed constitutive model is also described and defined.

Chapter 5 presents the experimental tests conducted to characterize the bladder wall during the development of this work. The experimental results are validated by comparison with literature published data. The proposed constitutive equation model is fitted to experimental results.

Chapter 6 includes the filling simulation of the bladder model, as well as the determination of the fibres representative orientations

Finally, in chapter 7 conclusions and future work suggestions are addressed.

Chapter 2

Bladder

During this chapter, the anatomy of the urinary bladder will be presented, as well as its function and relation with the rest of the urinary tract. The bladder wall will also be approached regarding its histology. Bladder clinical conditions and its repercussion on the normal behaviour of the urinary bladder will be addressed. Finally, the role of biomechanics in the study of the bladder will be discussed.

2.1 Anatomy

The bladder, or urinary bladder, is one the organs of which the urinary tract is composed. The urinary tract is divided in two sections, the upper and lower urinary tract. The upper tract contains the kidneys and two ureters, while the lower tract contains the bladder and urethra (and the prostate in males) [4], see figure 2.1. As a general overview, the function of the urinary tract is to balance fluids and remove wastes from blood. For this purpose, the blood flows through kidneys, that work as a filter aiming to remove waste substances from the blood stream and produce urine. The ureters serve as a connection between the kidneys and the bladder. As urine is produced, it is transported (by the means of the ureters) to the bladder where it is stored. The urine is finally expelled at an appropriate time, under a voluntary control via the urethra. This work will focus solely on the bladder [5, 4, 6].

The bladder is a hollow and highly distensible organ, where the anatomical position of the bladder varies depending on the degree of distension. An empty bladder, shaped like a three-sided pyramid (known as a flattened tetrahedron), is regarded as an extraperitoneal pelvic organ and lies behind the symphysis pubis. With an increase in distension (stimulated by the presence of urine) the bladder rises in a shape of a dome and becomes an abdominal organ. The bladder can be divided into three parts, the apex, a superior surface, two inferolateral surfaces, and the base, see figure 2.2. The base, shaped

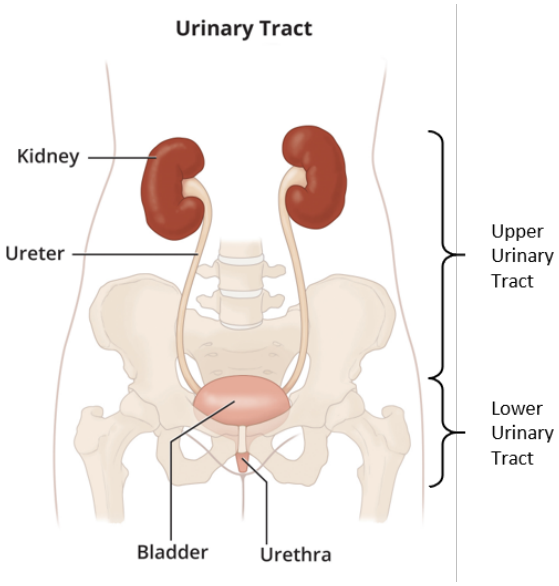

Figure 2.1: Urinary tract organs [5].

like an inverted triangle (trigone), has three openings, one at each of the triangle vertices. The two ureters enter the bladder at each of the upper corners of the base, while the lower corner opening, known as the internal urethral orifice, serves as a connection to the urethra, see figure 2.3. The apex of the bladder is directed to the top of the pubic symphysis, a structure known as the median umbilical ligament. The superior surface of the bladder is slightly domed when the bladder is empty, and as the bladder fills, the surface balloons upwards [4, 6, 1].

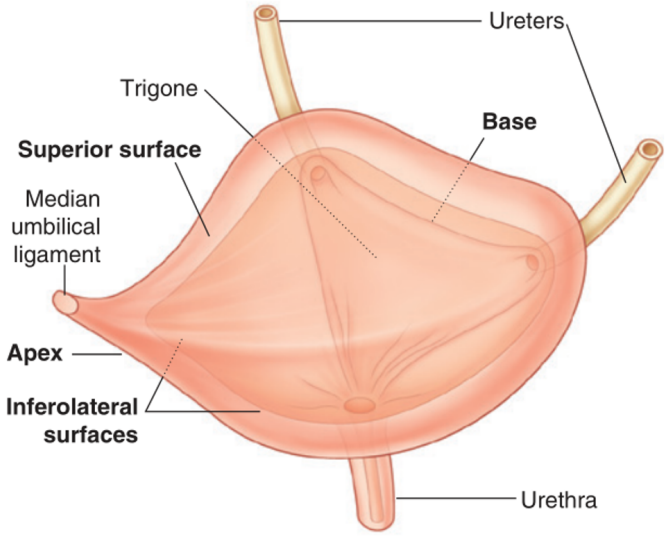

Figure 2.2: Superolateral view of the bladder [1].

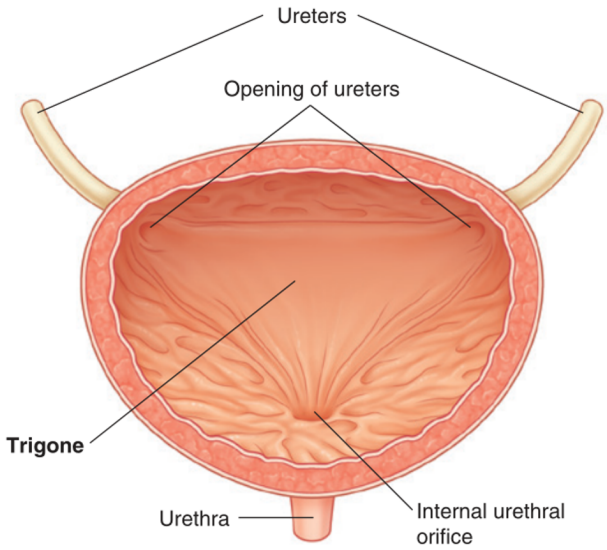

Figure 2.3: Bladder view cut with trigone representation [1].

Regarding the histology of the bladder, the bladder wall is a complex structure composed of four distinctive layers, see figure 2.4 [4, 7, 8, 9, 3].

- The **mucosa**, also known as the urothelium, which is the innermost layer composed of transitional epithelium cells that provides an elastic barrier that is impermeable to urine. When empty, the mucosa has numerous folds by the name of rugae that, in combination with the transitional epithelium allow the bladder to expand as it fills.

- The **submucosa**, is a thick layer of loose connective tissue, rich in elastin and collagen fibres, nerves, blood, and lymphatic vessels.

- The **detrusor**, which is a smooth muscular layer, that can be subdivided in three sublayers characterized by different orientation of muscular fibres. The internal one, where the fibres are found with a longitudinal orientation, from apex to base; The middle one, where fibres have a circular orientation (transverse to the latter) and an external sublayer, where the orientation is similar to the internal.

- The final and most external layer of the bladder is known as the **adventitia**, and is a visceral peritoneum. The mechanical contribution of this layer to the bladder wall properties is almost negligible.

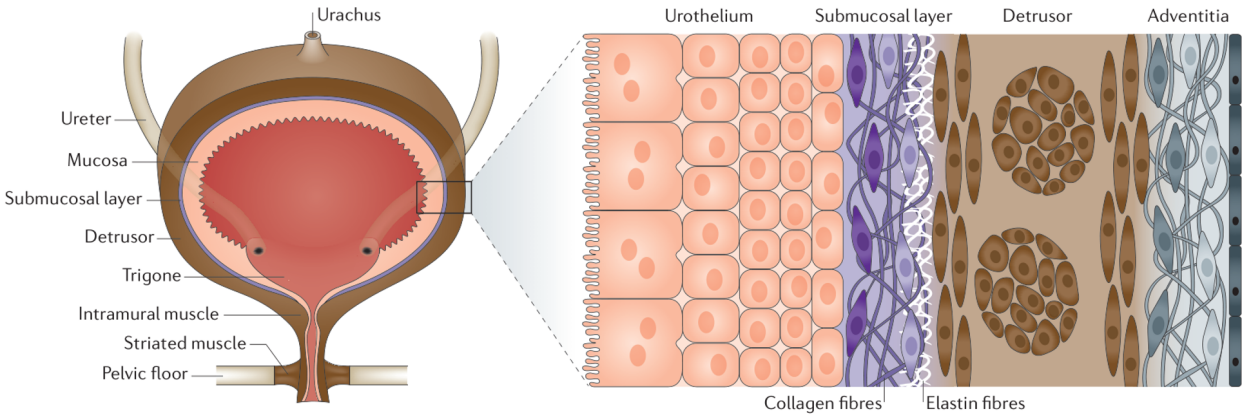

Figure 2.4: Bladder wall structure [7].

The average wall thickness of a human bladder is $3.3\,mm \pm 1.1\,mm$ for men and $3.0\,mm \pm 1.0\,mm$ for women, according to the study carried out by Hakenber *et al.* in [10]. The wall thickness is mostly uniform across the different parts of the organ, with exception of the trigone. Normal function bladder capacity increases with age, from childhood to adulthood. According to studies carried out in [11] and [12], during childhood the bladder capacity can be approximated by $(\text{years of age} + 2) * 30\,[ml]$ to adulthood, where the volume range from approximately 300 to 400 ml.

2.2 Bladder Clinical Conditions

A micturition cycle is referred to as the storage and voiding of urine from the bladder. Accordingly, the cycle has two stages, the storage and voiding phases. The first stage is done without any sensation as the bladder is filled with urine, while the bladder pressure is low. The ability to maintain a low pressure is due to the bladder high elasticity, consequence of being a highly distensible organ, also known as compliance. As the bladder continues to fill, the sensation of voiding starts to appear. The voiding phase, in a healthy bladder, being a voluntary act, can be delayed. Following a coordinated relaxation of the pelvic floor and sphincter muscles, the voiding phase is initiated [13, 14].

A healthy bladder is free of bacterial infection or tumours (that can lead to bladder cancer) and stores urine without discomfort. Healthy voiding occurs promptly with a strong continuous flow and complete emptying without pain or blood in urine. When, and if, necessary, an individual should be able to suspend voiding without urine leakage. Variation in these normal responses may be a sign of disease [13].

A number of conditions might cause a change on normal behaviour of the bladder, including overactive bladder, bladder outlet obstruction, bladder pain syndrome (formally known as interstitial cystitis), urinary tract infection, urinary incontinence and bladder cancers [13, 15].

2.3 Biomechanics of the Bladder

Biomechanics is the study of force, stress, deformation, and motion in biological structures and can be used to quantify and describe the intrinsic mechanical properties of many biological tissues. As a disease not only causes biological and functional alterations but also result in changes in the physical and structural properties of cells. Lekka *et al.* in [16] carried out a study to determine the elasticity of normal/healthy and cancerous human bladder epithelial cells, they found the Young's modulus of cancer cells to be about one-tenth of healthy cells. Studying diseases from a biomechanics perspective can lead to a better understanding of the pathophysiology (refers to the study of abnormal changes in body function that are the causes or consequences of disease processes) and pathogenesis (refers to the development of a disease and the chain of events leading to that disease) of a variety of diseases. Therefore, biomechanics provide an alternative and complementary approach to assess the onset or progression of diseases as well as to identify targets for therapeutic interventions [16, 17].

To study the bladder under a biomechanical approach, it is crucial to acknowledge the mechanical properties of the bladder tissue. Doing so, it would provide a thorough understanding of normal tissue function, which could be used in reconstructive biomedical modelling, to improve therapeutics and to further refine methods for tissue engineering and reconstructive urology [7]. However the characterization and modelling of the bladder wall has remained a challenge.

Through urodynamic studies, it is possible to evaluate changes in the compliance of the bladder wall, by testing the performance of the lower urinary tract. Cystometry, one of the urodynamic tests, is used to assess detrusor activity, sensation, capacity, pressure, urinary leakage, and compliance, to help to understand the patient's bladder abnormal behaviour during filling-voiding cycles, helping the diagnose of incontinence, overactive bladder, infections and other urine control related problems. It is performed by the means of a catheter, placed into the bladder which is an invasive technique used to fill the bladder and to measure the bladder capacity, the pressure at different filling volumes, urge to void and leakage points [7]. However, an important tool for *in vivo* (latin for "within the living") diagnoses, independently it can not assess changes in the bladder wall properties. To collect more information about the mechanical properties of the bladder there is a need for *ex vivo* (latin for "outside the living") tests, namely uniaxial and biaxial mechanical tests, performed on samples extracted from the bladder tissue wall. Chapter 5 presented the uniaxial tests performed during this work.

The role of biomechanical models is to accurately describe the biological tissues behaviour, in the scope of this work, the bladder.

Chapter 3

Continuum Mechanics

This chapter presents fundamental concepts of continuum mechanics. First the basics assumption underlying the application of this theory will be announced. Then, the major kinematics variables will be along with common strain and stress measures. Polar decomposition of the motion, as well as volume and surface deformations will also be address. Material response to deformation, behaviour regarding volume changes and dependency on orientation. Finally, fibre dispersion will be addressed.

3.1 Continuum Mechanics Theory

At a microscopic level, materials show an heterogeneous atomic structure, composed of molecules formed by atomic and subatomic particles, thus matter is not continuous. An atomistic approach has in consideration the material structure, which for common engineering application becomes too complex and not adequate.
Continuum mechanics theory studies the behaviour of materials without detailed knowledge of their microscopic structure. It regards matter as indefinitely divisible, where a particle is considered an infinitesimal volume of material. The applicability of this theory depends on the given situation, as it cannot be used in nanomechanics, where the nanoscale is studied.
The main objective of continuum mechanics is to study the response of materials to different loading conditions, based on two major parts. General principles axioms, for instance the balance of linear momentum, and constitutive equations defined to idealize the response of a material [18, 19, 20].

3.2 Kinematics

Let **B** be a deformable body in a domain $\Omega \subset R^3$. Considering $\mathbf{B}_0$ the initial, or reference, configuration, the body may undergo a motion, assuming motion with deformation, at any given time, t, transforming the initial configuration into $\mathbf{B}_t$ denoted by a mapping φ. As shown in figure 3.1: The position of any material point, P in figure 3.2, on the reference

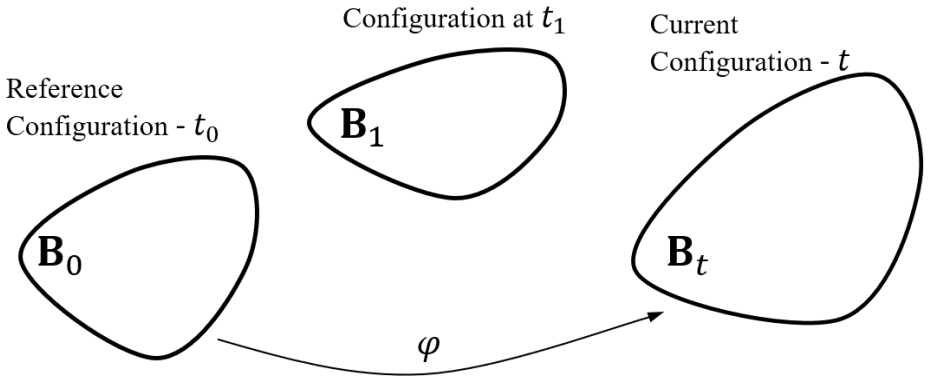

Figure 3.1: Motion of a body.

configuration $\mathbf{B}_0$ can be defined by $\mathbf{X} = [X_1, X_2, X_3]$. Following the motion mapped by φ, the current position of any material point, Q , is identified by $\mathbf{x} = [x_1, x_2, x_3]$, written as:

$$\mathbf{x} = \varphi(\mathbf{X}, t) \tag{3.1}$$

Assuming the motion mapping, φ, is invertible, the position $\mathbf{X}$ can be given in relation to the position at any given time, $\mathbf{x}$, by:

$$\mathbf{X} = \varphi^{-1}(\mathbf{x}, t) \tag{3.2}$$

The displacement, $\mathbf{u}(\mathbf{X}, t)$, can then be given by:

$$\mathbf{u}(\mathbf{X}, t) = \varphi(\mathbf{X}, t) - \mathbf{X} = \mathbf{x} - \mathbf{X} \tag{3.3}$$

Represented in figure 3.2, P' and Q' are adjacent points at infinitesimal distances from P and Q, respectively, denoted by the differential element vectors $d\mathbf{X}$ and $d\mathbf{x}$. Assuming a continuous mapping, the relationship between these vectors can be given as:

$$d\mathbf{x} = \frac{\partial \mathbf{x}}{\partial \mathbf{X}} d\mathbf{X} \Longrightarrow d\mathbf{x} = \mathbf{F} d\mathbf{X} \tag{3.4}$$

where **F** is known as the deformation gradient, expressed as:

$$F_{ij} = \frac{\partial x_i}{\partial X_j} \tag{3.5}$$

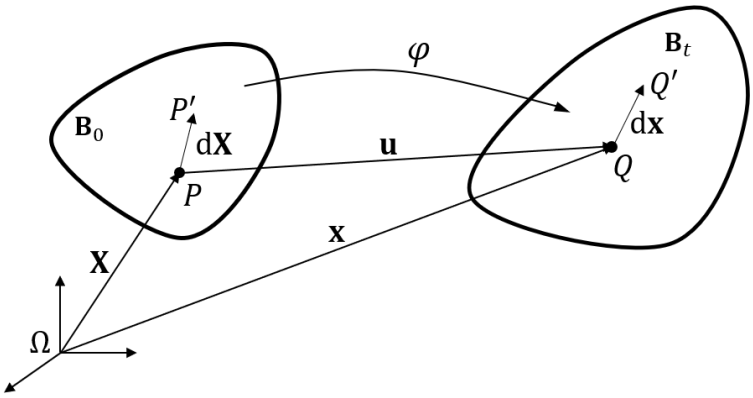

Figure 3.2: Reference and current configuration.

It can also be rewritten as:

$$\mathbf{F} = \mathbf{I} + \frac{\partial \mathbf{u}}{\partial \mathbf{X}} = \mathbf{I} + \nabla_X \mathbf{u} \tag{3.6}$$

where $\partial \mathbf{u}/\partial \mathbf{X}$ is known as the displacement gradient. An infinitesimal volume can increase or decreasing during the motion; however, it cannot decrease to a point. Mathematically this can be translated so that the determinant of the deformation gradient must be greater than zero, meaning that the volume ratio is different than zero.

$$\det \mathbf{F} \equiv J > 0 \tag{3.7}$$

The determinant of the deformation matrix is also known as the Jacobian determinant, J [18, 19, 20].

3.3 Lagrangian and Eulerian Strains

3.3.1 Lagrangian Strain

Lagrangian strain uses the initial, also known as material, configuration as a reference. Recall that the $d\mathbf{X}$ is transformed into $d\mathbf{x}$. The change in the squared length of these two vectors can be given by:

$$\begin{aligned} \|d\mathbf{x}\|^2 - \|d\mathbf{X}\|^2 &= d\mathbf{x}^{\mathrm{T}} d\mathbf{x} - d\mathbf{X}^{\mathrm{T}} d\mathbf{X} \\ &= d\mathbf{X}^{\mathrm{T}} \mathbf{F}^{\mathrm{T}} \mathbf{F} d\mathbf{X} - d\mathbf{X}^{\mathrm{T}} d\mathbf{X} \\ &= d\mathbf{X}^{\mathrm{T}} \left(\mathbf{F}^{\mathrm{T}} \mathbf{F} - \mathbf{I} \right) d\mathbf{X} \end{aligned} \tag{3.8}$$

The quantity $\left(\mathbf{F}^{\mathrm{T}}\mathbf{F} - \mathbf{I}\right)$ measures the change in square length with respect to the initial vector length. The term $\mathbf{F}^{\mathrm{T}}\mathbf{F}$ is defined as the right Cauchy-Green deformation tensor:

$$\mathbf{C} = \mathbf{F}^{\mathrm{T}} \mathbf{F} \tag{3.9}$$

From equation 3.8 the Lagrangian strain can be defined as:

$$\mathbf{E} = \frac{1}{2}\left(\mathbf{C} - \mathbf{I}\right) \tag{3.10}$$

the normalization factor, $1/2$, was introduced to make the definition identical to the engineering strains in the case of infinitesimal strains. The Lagrangian strain can also be written in terms of displacement gradient [20],

$$\mathbf{E} = \frac{1}{2}\left(\frac{\partial \mathbf{u}}{\partial \mathbf{X}} + \frac{\partial \mathbf{u}^{\mathrm{T}}}{\partial \mathbf{X}} + \frac{\partial \mathbf{u}^{\mathrm{T}}}{\partial \mathbf{X}}\frac{\partial \mathbf{u}}{\partial \mathbf{X}}\right) = \frac{1}{2}\left(\nabla_X \mathbf{u} + \nabla_X \mathbf{u}^{\mathrm{T}} + \nabla_X \mathbf{u}^{\mathrm{T}} \nabla_X \mathbf{u}\right) \tag{3.11}$$

3.3.2 Eulerian Strain

Eulerian strain uses the deformed, or spatial, configuration as a reference. Writing again the change in the square length of the vectors $d\mathbf{x}$ and $d\mathbf{X}$,

$$\begin{aligned} \|d\mathbf{x}\|^2 - \|d\mathbf{X}\|^2 &= d\mathbf{x}^{\mathrm{T}} d\mathbf{x} - d\mathbf{X}^{\mathrm{T}} d\mathbf{X} \\ &= d\mathbf{x}^{\mathrm{T}} d\mathbf{x} - d\mathbf{x}^{\mathrm{T}} \mathbf{F}^{-\mathrm{T}} \mathbf{F}^{-1}\, \mathrm{d}\mathbf{x} \\ &= d\mathbf{x}^{\mathrm{T}} \left(\mathbf{I} - \mathbf{F}^{-\mathrm{T}} \mathbf{F}^{-1}\right) d\mathbf{x} \end{aligned} \tag{3.12}$$

the quantity $\left(\mathbf{I} - \mathbf{F}^{-T}\mathbf{F}^{-1}\right)$ measures the change in squared length with respect to the deformed vector length. The term $\mathbf{F}\mathbf{F}^{\mathrm{T}}$ is defined as the left Cauchy-Green deformation tensor:

$$\mathbf{b} = \mathbf{F}\mathbf{F}^{\mathrm{T}} \tag{3.13}$$

The Eulerian strain can now be defined using the left Cauchy-Green tensor as

$$\mathbf{e} = \frac{1}{2}\left(\mathbf{I} - \mathbf{b}^{-1}\right) \tag{3.14}$$

Or, in terms of the displacement gradient [20],

$$\mathbf{e} = \frac{1}{2}\left(\frac{\partial \mathbf{u}}{\partial \mathbf{x}} + \frac{\partial \mathbf{u}^{\mathrm{T}}}{\partial \mathbf{x}} - \frac{\partial \mathbf{u}^{\mathrm{T}}}{\partial \mathbf{x}}\frac{\partial \mathbf{u}}{\partial \mathbf{x}}\right) = \frac{1}{2}\left(\nabla_x \mathbf{u} + \nabla_x \mathbf{u}^{\mathrm{T}} + \nabla_x \mathbf{u}^{\mathrm{T}} \nabla_x \mathbf{u}\right) \tag{3.15}$$

3.4 Polar Decomposition

Motion can be divided into pure stretches and pure rotation by polar decomposition. As the determinant of the deformation matrix is greater than zero, $\det \mathbf{F} > 0$, meaning that $\mathbf{F}$ is non-singular, it exists a proper-orthogonal second order tensor, $\mathbf{R}$, know as the rotation tensor, such that:

$$\mathbf{F} = \mathbf{R}\mathbf{U} = \mathbf{V}\mathbf{R} \tag{3.16}$$

where **RU** is the right polar decomposition and **VR** is the left polar decomposition. **U** and **V** are positive-definite symmetric second order tensors, known as:

- **U** the right stretch tensor, the Lagrangian tensor, or the material stretch tensor.
- **V** the left stretch tensor, the Eulerian tensor, or the spatial stretch tensor.

If a transformation with just strain is carried out first and only then a transformation with rotation is it referred to as a right polar decomposition. Whilst in the left polar decomposition, it is first carried out an orthogonal transformation, rotation, and then transformation only with strain is applied. Applying the scalar product between $\mathbf{F}^{\mathrm{T}}$ and the right polar decomposition, it can be written [18, 20],

$$\mathbf{F}^{\mathrm{T}}\mathbf{F} = \mathbf{F}^{\mathrm{T}}\mathbf{R}\mathbf{U} \Longrightarrow \mathbf{C} = \mathbf{F}^{\mathrm{T}}\mathbf{R}\mathbf{U} = \mathbf{U}^{\mathrm{T}}\mathbf{U} \Leftrightarrow \mathbf{C} = \mathbf{U}^2 \tag{3.17}$$

3.5 Volume and Surface Deformation

3.5.1 Volume Changes

The change in volume in large deformations cannot be negligible. Depending on the material, different behaviours can be seen when subjected to volume-changing deformation, known as dilatation, or volume-preserving deformation, known as distortion. Hence, the importance of expressing the volume changes, even if some cases are known as incompressible or nearly incompressible. Considering an infinitesimal element volume composed of three vectors, $\left(d\mathbf{X}^1, d\mathbf{X}^2, d\mathbf{X}^3\right)$, the infinitesimal undeformed initial volume, dV_0 is given by:

$$dV_0 = d\mathbf{X}^1 \cdot \left(d\mathbf{X}^2 \times d\mathbf{X}^3\right) \tag{3.18}$$

which is deformed to dV_t, written as:

$$dV_t = d\mathbf{x}^1 \cdot \left(d\mathbf{x}^2 \times d\mathbf{x}^3\right) \tag{3.19}$$

The relation between the two volumes, using the definition of the deformation gradient, $d\mathbf{x} = \mathbf{F}d\mathbf{X}$, can be given by:

$$dV_t = JdV_0 \tag{3.20}$$

once again, it is notable how the Jacobian determinant, $J = \det \mathbf{F}$, represents the volume ratio [20].

3.5.2 Area Changes

Surface area changes can also be expressed in terms of deformation. Let **N** be unit normal vector of an infinitesimal area, undeformed, dS_0, with the edges being given by $d\mathbf{X}^1$ and $d\mathbf{X}^2$, on and undeformed surface S_0. After being subjected to a motion ruled by a

deformation gradient **F** , the deformed surface S_t is now denoted by, **n**, dS_x, $d\mathbf{x}^1$ and $d\mathbf{x}^2$, respectively, as shown in Figure 3.3. Once again, the objective is to find the relation be-

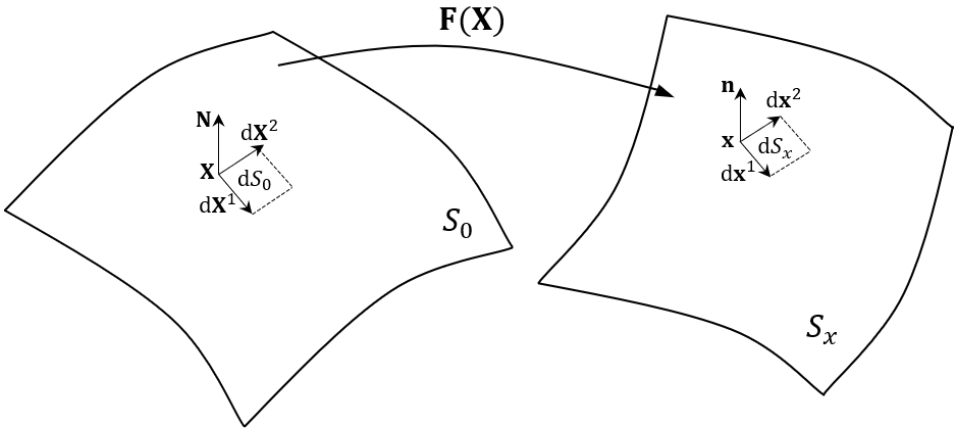

Figure 3.3: Undeformed and deformed surfaces.

tween the two areas. The deformed edges, $d\mathbf{x}^1$ and $d\mathbf{x}^2$, can be represented in terms of the deformation gradient, as:

$$\begin{aligned} d\mathbf{x}^1 &= \mathbf{F}d\mathbf{X}^1 \\ d\mathbf{x}^2 &= \mathbf{F}d\mathbf{X}^2 \end{aligned} \tag{3.21}$$

The infinitesimal areas can be written by using a vector product given by:

$$\begin{aligned} \mathbf{N}dS_0 &= d\mathbf{X}^1 \times d\mathbf{X}^2 \\ \mathbf{n}dS_x &= d\mathbf{x}^1 \times d\mathbf{x}^2 \end{aligned} \tag{3.22}$$

It can now be written that,

$$\mathbf{n}dS_x = J\mathbf{F}^{-T}\mathbf{N}dS_0 \tag{3.23}$$

The explicit form of **n** can be obtained as:

$$\mathbf{n} = \frac{\mathbf{F}\left(\mathbf{x}\right)^{-T}\mathbf{N}\left(\mathbf{X}\right)}{\|\mathbf{F}\left(\mathbf{x}\right)^{-T}\mathbf{N}\left(\mathbf{X}\right)\|} \tag{3.24}$$

By substituting equation 3.24 into 3.23, the relation between both surface areas can be obtained as [20]:

$$dS_x = J\|\mathbf{F}\left(\mathbf{x}\right)^{-T}\mathbf{N}\left(\mathbf{X}\right)\|dS_0 \tag{3.25}$$

3.6 Cauchy and Piola-Kirchhoff Stress Tensors

Similar to strain, stress also depends on its reference, as different stresses can be defined based on the reference used. Stress is defined by a force acting on an infinitesimal area.

In linear analyses, as the area remained unaltered because of the infinitesimal deformation assumption, it was not necessary to distinguish from deformed or undeformed area. However, this is not the case in problems characterized by large deformations, so it is important to define the area used to determine the stress [20].

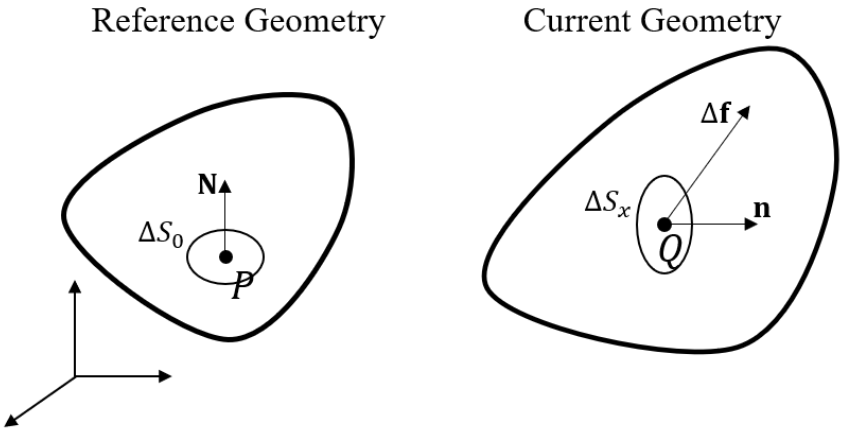

Figure 3.4: Stress vectors in the initial and deformed geometries.

From the current geometry, Figure 3.4, the stress vector at any point Q can be written depending on the deformed area of the differential element ΔS_x , the acting force $\Delta \mathbf{f}$ and the unit normal $\mathbf{n}$ of the deformed geometry.

$$\mathbf{t} = \lim_{\Delta S_x \to 0} \left(\frac{\Delta \mathbf{f}}{\Delta S_x} \right) = \boldsymbol{\sigma} \mathbf{n} \tag{3.26}$$

where $\boldsymbol{\sigma}$ is known as the Cauchy stress tensor, and it refers to the current, deformed, geometry as a reference for both force and area. Given so, it is referred to as the *true stress*.

However, a different stress vector can be defined, considering the same force, although considering the initial, undeformed, area ΔS_0 and the unit normal $\mathbf{N}$ in the undeformed geometry. It is defined as:

$$\mathbf{T} = \lim_{\Delta S_0 \to 0} \left(\frac{\Delta \mathbf{f}}{\Delta S_0} \right) = \mathbf{P}^{\mathrm{T}} \mathbf{N} \tag{3.27}$$

where $\mathbf{P}$ is known as the first Piola-Kirchhoff stress tensor, and it refers to the current, deformed, geometry for the force, however the area refers to the initial geometry.

The unit normal $\mathbf{n}$ its related to is predecessor $\mathbf{N}$ in the initial geometry. If so, the first Piola-Kirchhoff stress is also related to the Cauchy stress. The infinitesimal force can be given in the terms of both stresses by:

$$d\mathbf{f} = \boldsymbol{\sigma} \mathbf{n} dS_x = \mathbf{P}^{\mathrm{T}} \mathbf{N} dS_0 \tag{3.28}$$

Using the relation between the unit normal vectors, it can be written:

$$\mathbf{P} = J\mathbf{F}^{-1}\boldsymbol{\sigma} \tag{3.29}$$

Unlike the Cauchy stress tensor, the first Piola-Kirchhoff is not symmetric, however by post-multiplying **P** with the transpose of the inverse of the deformation gradient, **F**, it can be obtained a symmetric tensor. The resultant tensor is called the second Piola-Kirchhoff stress tensor and is denoted by **S**.

$$\mathbf{S} = \mathbf{P}\mathbf{F}^{-T} = J\mathbf{F}^{-1}\boldsymbol{\sigma}\mathbf{F}^{-\mathrm{T}} \tag{3.30}$$

Equation 3.30 can be rearranged so that the Cauchy stress tensor can be obtained by:

$$\boldsymbol{\sigma} = J^{-1}\mathbf{F}\mathbf{S}\mathbf{F}^{\mathrm{T}} \tag{3.31}$$

The multiplying factor, J^{-1} is related to the volume change between the undeformed and deformed geometries. As it depends on the deformation, it is inconvenient to calculate stress based on it. Therefore, a new stress measure can be defined $\boldsymbol{\tau}$, called Kirchhoff stress, given by [18, 19, 20]:

$$\boldsymbol{\tau} = J\boldsymbol{\sigma} = \mathbf{F}\mathbf{S}\mathbf{F}^{\mathrm{T}} \tag{3.32}$$

3.7 Tangent Matrix

The rate of change of the second Piola-Kirchhoff tensor, $\dot{\mathbf{S}}$, can be expressed as:

$$\dot{\mathbf{S}} = \frac{\partial^2\Psi(\mathbf{E})}{\partial\mathbf{E}\otimes\partial\mathbf{E}} : \dot{\mathbf{E}} = \mathbb{C}^{\tan} : \dot{\mathbf{E}} \tag{3.33}$$

where $\dot{\mathbf{S}}$ and $\dot{\mathbf{E}}$ are objective rates, and $\mathbb{C}^{\tan}$ is a fourth-order tensor known as the material elastic tangent stiffness tensor also called tangent matrix. Recalling and rearranging equation 3.10 it can be written that:

$$2\mathbf{E} = (\mathbf{C} - \mathbf{I}) \Longrightarrow 2\dot{\mathbf{E}} = \dot{\mathbf{C}} \tag{3.34}$$

therefore,

$$\dot{\mathbf{S}} = 2\frac{\partial^2\Psi(\mathbf{C})}{\partial\mathbf{C}\otimes\partial\mathbf{C}} : \dot{\mathbf{C}} \Longrightarrow \dot{\mathbf{S}} = \underbrace{4\frac{\partial^2\Psi(\mathbf{C})}{\partial\mathbf{C}\otimes\partial\mathbf{C}}}_{=\mathbb{C}^{\tan}} : \dot{\mathbf{E}} \tag{3.35}$$

Accordingly, the tangent matrix $\mathbb{C}^{\tan}$ can be defined as [18]:

$$\mathbb{C}^{\tan} = 4\frac{\partial^2\Psi(\mathbf{C})}{\partial\mathbf{C}\otimes\partial\mathbf{C}} = 2\frac{\partial\mathbf{S}}{\partial\mathbf{C}} \tag{3.36}$$

3.8 Constitutive Equations

The purpose of constitutive equations is to establish the relation between two physical quantities, for example, between stress and strain. They can also be described as a way of idealizing the response of a material. Over the years there has been an extensive development of different constitutive models.

3.8.1 Hyperelasticity

An hyperelastic material is defined as a material in which the expected deformation is the same if the final load is the same, meaning that it is independent on the deformation history. An hyperelastic material can be subjected to large deformations without any internal energy dissipation, being capable of returning to their initial state as the load disappears. A constitutive model for an hyperelastic material is characterized by a function known as Helmholtz free energy per unit reference of volume Ψ, also known as strain-energy function. For hyperelastic materials, the strain function is only dependent on the deformation gradient, $\Psi = \Psi(\mathbf{F})$. In pure deformation processes, not affected by entropy or temperature, the internal energy dissipation, $\mathcal{D}_{int}$, is equal to zero, thus a reversible process. From the Clausius-Planck inequality, for a reversible process, it can be written [18]:

Current configuration:

$$\mathcal{D}_{int} = \boldsymbol{\sigma} : \mathbf{D} - \dot{\Psi} = 0 \Rightarrow \dot{\Psi} = \boldsymbol{\sigma} : \mathbf{D} \tag{3.37}$$

Initial configuration:

$$\begin{aligned} \mathcal{D}_{int} &= \mathbf{P} : \dot{\mathbf{F}} - \dot{\Psi} = 0 \Rightarrow \dot{\Psi} = \mathbf{P} : \dot{\mathbf{F}} \\ &= \frac{1}{2}\mathbf{S} : \dot{\mathbf{C}} - \dot{\Psi} = 0 \Rightarrow \dot{\Psi} = \frac{1}{2}\mathbf{S} : \dot{\mathbf{C}} \end{aligned} \tag{3.38}$$

where $\boldsymbol{\sigma}$ is the Cauchy stress tensor, $\mathbf{D}$ is the rate-of-deformation tensor, $\mathbf{P}$ is the first Piola-Kirchhoff stress tensor, $\mathbf{S}$ is the second Piola-Kirchhoff stress tensor and $\mathbf{C}$ is the right Cauchy-Green deformation tensor.
$\dot{\Psi} = \dot{\Psi}(\mathbf{F})$, known as the rate of change of the strain-energy is given by:

$$\dot{\Psi}(\mathbf{F}) = \frac{\partial \Psi(\mathbf{F})}{\partial \mathbf{F}} : \frac{\partial \mathbf{F}}{\partial t} = \frac{\partial \Psi(\mathbf{F})}{\partial \mathbf{F}} : \dot{\mathbf{F}} \tag{3.39}$$

By substituting it in the equation 3.38, using the first Piola-Kirchhoff stress tensor, it is obtained:

$$\mathbf{P} : \dot{\mathbf{F}} - \frac{\partial \Psi(\mathbf{F})}{\partial \mathbf{F}} : \dot{\mathbf{F}} = 0 \Rightarrow \mathbf{P} : \dot{\mathbf{F}} = \frac{\partial \Psi(\mathbf{F})}{\partial \mathbf{F}} : \dot{\mathbf{F}} \Rightarrow \mathbf{P} = \frac{\partial \Psi(\mathbf{F})}{\partial \mathbf{F}} \tag{3.40}$$

The strain is objective, meaning it must be the same for any observer, thus accordingly to that $\Psi(\mathbf{F}) = \Psi(\mathbf{F}^*) = \Psi(\mathbf{Q} \cdot \mathbf{F})$, where $\mathbf{Q}$ is an orthogonal tensor. Following the polar decomposition, where $\mathbf{F} = \mathbf{RU}$, and by adopting $\mathbf{Q} = \mathbf{R}^{\mathrm{T}}$, it can be obtained:

$$\begin{aligned} \Psi(\mathbf{F}) &= \Psi(\mathbf{Q} \cdot \mathbf{F}) \\ &= \Psi(\mathbf{Q} \cdot \mathbf{R} \cdot \mathbf{U}) \\ &= \Psi(\mathbf{U}) \end{aligned} \tag{3.41}$$

where $\mathbf{U}$ is the right stretch tensor. Since $\mathbf{C}$, the right Cauchy-Green deformation tensor, can be directly linked to $\mathbf{U}$, as $\mathbf{C} = \mathbf{U}^2$. Therefore, the strain-energy function can also be given in terms of $\mathbf{C}$ as $\Psi(\mathbf{C})$. The rate of change of the strain-energy can now be given by:

$$\dot{\Psi}(\mathbf{C}) = \frac{\partial \Psi(\mathbf{C})}{\partial \mathbf{C}} : \frac{\partial \mathbf{C}}{\partial t} = \frac{\partial \Psi(\mathbf{C})}{\partial \mathbf{F}} : \dot{\mathbf{C}} \tag{3.42}$$

Substituting equation 3.42 into the internal energy configuration, in form of the initial configuration, from equation 3.38, it can be obtained:

$$\begin{aligned} \mathcal{D}_{\text{int}} &= \frac{1}{2}\mathbf{S} : \dot{\mathbf{C}} - \dot{\Psi}(\mathbf{C}) = 0 \\ &= \frac{1}{2}\mathbf{S} : \dot{\mathbf{C}} - \frac{\partial \Psi(\mathbf{C})}{\partial \mathbf{C}} : \dot{\mathbf{C}} = 0 \\ &= \left(\frac{1}{2}\mathbf{S} - \frac{\partial \Psi(\mathbf{C})}{\partial \mathbf{C}}\right) : \dot{\mathbf{C}} = 0 \end{aligned} \tag{3.43}$$

In a mechanical process with $\dot{\mathbf{C}} \neq 0$, the final condition from equation 3.43 remains valid only if:

$$\left(\frac{1}{2}\mathbf{S} - \frac{\partial \Psi(\mathbf{C})}{\partial \mathbf{C}}\right) = 0 \Rightarrow \mathbf{S} = 2\frac{\partial \Psi(\mathbf{C})}{\partial \mathbf{C}} \tag{3.44}$$

As the Cauchy stress tensor can be defined in terms of $\mathbf{S}$, from equation 3.31, $\boldsymbol{\sigma} = J^{-1}\mathbf{FSF}^{\mathrm{T}}$, it can also be defined in terms of the strain-energy function, Ψ, using the relation from equation 3.44, [18, 19, 20].

$$\boldsymbol{\sigma} = 2J^{-1}\mathbf{F}\frac{\partial \Psi(\mathbf{C})}{\partial \mathbf{C}}\mathbf{F}^{\mathrm{T}} \tag{3.45}$$

3.8.2 Incompressible Materials

As many materials can be subjected to large deformations without any volume change, they are considered incompressible. As presented previously, the volume ratio is characterized by J , thus for an incompressible material, it is given:

$$J = \det \mathbf{F} = 1 \tag{3.46}$$

The strain-energy function can be decomposed in two distinctive parts. The first one, Ψ_{iso}, describes the isochoric elastic response and the second one, Ψ_{vol}, describes the volumetric elastic response, so that:

$$\begin{aligned} \Psi(\mathbf{F}) &= \Psi_{\text{iso}}(\mathbf{F}) + \Psi_{\text{vol}}(J) \\ \Psi(\mathbf{C}) &= \Psi_{\text{iso}}(\mathbf{C}) + \Psi_{\text{vol}}(J) \end{aligned} \tag{3.47}$$

where:

$$\Psi_{\text{vol}} = p\,(1 - J) \tag{3.48}$$

The volumetric response is responsible to impose the incompressibility of the material. The first Piola-Kirchhoff stress tensor, $\mathbf{P}$, can be written, following equation 3.40 as:

$$\mathbf{P} = \frac{\partial \Psi\,(\mathbf{F})}{\partial \mathbf{F}} - p\mathbf{F}^{\mathrm{T}} \tag{3.49}$$

From equations 3.30 and 3.44 it is possible to define the second Piola-Kirchhoff stress tensor, $\mathbf{S}$, given by [18, 19, 20]:

$$\mathbf{S} = 2\frac{\partial \Psi\,(\mathbf{C})}{\partial \mathbf{C}} - p\mathbf{F}^{-1}\mathbf{F}^{\mathrm{T}} \Leftrightarrow \mathbf{S} = 2\frac{\partial \Psi\,(\mathbf{C})}{\partial \mathbf{C}} - p\mathbf{C}^{-1} \tag{3.50}$$

To avoid numerical complications in computational analysis, the incompressibility behaviour is imposed by what is known as the penalty method, based on the idea that an incompressible material can be modelled by using very large bulk modulus, as used during this work. Consequently, the strain energy function has an additional contribution with a penalty function,Ψ_{pen}, without any physical meaning, given by [19],

$$\Psi_{\text{pen}} = \frac{1}{\mathrm{D}_1}\,(J - 1)^2 \tag{3.51}$$

3.8.3 Compressible Materials

Unlike incompressible materials, some can experience a change of volume when subjected to large deformations. The volumetric part of the strain-energy function Ψ_{vol} is responsible not only to impose the incompressibility but also to account for compressibility. The deformation gradient, $\mathbf{F}$, and the right Cauchy-Green tensor $\mathbf{C}$, can be decomposed into a volume preserving component and a volume changing component. The part associated with volume preserving deformations are the so called, modified deformation gradient, $\overline{\mathbf{F}}$, and modified right Cauchy-Green tensor, $\overline{\mathbf{C}}$ [18, 19, 20], given by:

$$\overline{\mathbf{F}} = J^{-\frac{1}{3}}\mathbf{F} \quad \wedge \quad \overline{\mathbf{C}} = J^{-\frac{1}{3}}\mathbf{C} \tag{3.52}$$

The isochoric part of the strain-energy function, Ψ_{iso}, is now evaluated on the modified tensor presented previously. Following so, that strain-energy function is then given by:

$$\begin{aligned}\Psi(\mathbf{F}) &= \Psi_{\text{iso}}(\overline{\mathbf{F}}) + \Psi_{\text{vol}}(J)\\ \Psi(\mathbf{C}) &= \Psi_{\text{iso}}(\overline{\mathbf{C}}) + \Psi_{\text{vol}}(J)\end{aligned} \tag{3.53}$$

3.8.4 Isotropic Material

A material is considered isotropic when their properties and response is the same in all directions, therefore being independent on the direction [19].

Considering the material configuration, the strain-energy function, Ψ, in function of the right Cauchy-Green tensor, $\mathbf{C}$, must be independent on the material orientation. Accordingly, Ψ must only be a function of the invariants of $\mathbf{C}$:

$$\Psi(\mathbf{C}) = \Psi(\mathrm{I}_1, \mathrm{I}_2, \mathrm{I}_3) \tag{3.54}$$

Where the invariants of $\mathbf{C}$ are defined as:

$$\mathrm{I}_1 = \mathrm{tr}\,(\mathbf{C}) \tag{3.55a}$$

$$\mathrm{I}_2 = \frac{1}{2}\left(\mathrm{I}_1^2 - \mathbf{C}:\mathbf{C}\right) \tag{3.55b}$$

$$\mathrm{I}_3 = \det(\mathbf{C}) \tag{3.55c}$$

The derivative of the strain-energy function with respect to $\mathbf{C}$, $\Psi(\mathbf{C})$, can be written following the chain rule, as:

$$\frac{\partial \Psi(\mathbf{C})}{\partial \mathbf{C}} = \frac{\partial \Psi}{\partial \mathrm{I}_1}\frac{\partial \mathrm{I}_1(\mathbf{C})}{\partial \mathbf{C}} + \frac{\partial \Psi}{\partial \mathrm{I}_2}\frac{\partial \mathrm{I}_2(\mathbf{C})}{\partial \mathbf{C}} + \frac{\partial \Psi}{\partial \mathrm{I}_3}\frac{\partial \mathrm{I}_3(\mathbf{C})}{\partial \mathbf{C}} = \sum_{a=1}^{3}\frac{\partial \Psi}{\partial \mathrm{I}_a}\frac{\partial \mathrm{I}_a}{\partial \mathbf{C}} \tag{3.56}$$

where the derivatives of the invariants with respect to $\mathbf{C}$, as written as:

$$\frac{\partial \mathrm{I}_1}{\partial \mathbf{C}} = \frac{\partial\, \mathrm{tr}\mathbf{C}}{\partial \mathbf{C}} = \frac{\partial(\mathbf{I}:\mathbf{C})}{\partial \mathbf{C}} = \mathbf{I} \tag{3.57a}$$

$$\frac{\partial \mathrm{I}_2}{\partial \mathbf{C}} = \frac{1}{2}\left(2\,\mathrm{tr}\mathbf{C}\,\mathbf{I} - \frac{\partial\, \mathrm{tr}\left(\mathbf{C}^2\right)}{\partial \mathbf{C}}\right) = \mathrm{I}_1\mathbf{I} - \mathbf{C} \tag{3.57b}$$

$$\frac{\partial \mathrm{I}_3}{\partial \mathbf{C}} = \mathrm{I}_3\mathbf{C}^{-1} \tag{3.57c}$$

Substituting the derivatives, given by equation 3.57, in equation 3.56, is possible to obtain the second Piola-Kirchhoff stress tensor $\mathbf{S}$, recalling equation 3.44, as:

$$\mathbf{S} = 2\left[\left(\frac{\partial \Psi}{\partial \mathrm{I}_1} + \mathrm{I}_1\frac{\partial \Psi}{\partial \mathrm{I}_2}\right)\mathbf{I} - \frac{\partial \Psi}{\partial \mathrm{I}_2}\mathbf{C} + \mathrm{I}_3\frac{\partial \Psi}{\partial \mathrm{I}_3}\mathbf{C}^{-1}\right] \tag{3.58}$$

The Cauchy stress tensor, $\boldsymbol{\sigma}$, referred to as the spatial counterpart of $\mathbf{S}$, given by equation 3.45 can now be written as:

$$\boldsymbol{\sigma} = 2\,\mathrm{J}^{-1}\left[\left(\frac{\partial \Psi}{\partial \mathrm{I}_1} + \mathrm{I}_1\frac{\partial \Psi}{\partial \mathrm{I}_2}\right)\mathbf{b} - \frac{\partial \Psi}{\partial \mathrm{I}_2}\mathbf{b}^2 + \mathrm{I}_3\frac{\partial \Psi}{\partial \mathrm{I}_3}\mathbf{I}\right] \tag{3.59}$$

where $\mathbf{b} = \mathbf{F}\mathbf{F}^T$ from equation 3.13, is the left Cauchy-Green tensor.
This equation is using the derivatives with respect to $\mathbf{C}$, however for a material to be isotropic, $\Psi(\mathbf{C})$ must satisfy the following:

$$\Psi(\mathbf{C}) = \Psi\left(\mathbf{Q}\cdot\mathbf{C}\cdot\mathbf{Q}^{\mathrm{T}}\right) \tag{3.60}$$

For any orthogonal tensor $\mathbf{Q}$. Following the Polar Decomposition presented in section 3.4, it the rotation tensor is used, $\mathbf{Q} = \mathbf{R}$, it can be obtained:

$$\begin{aligned}\Psi(\mathbf{C}) &= \Psi\left(\mathbf{R}\cdot\mathbf{C}\cdot\mathbf{R}^{\mathrm{T}}\right) = \Psi\left(\mathbf{R}\cdot\mathbf{F}^{\mathrm{T}}\cdot\mathbf{F}\cdot\mathbf{R}^{\mathrm{T}}\right) = \Psi\left(\mathbf{V}^{\mathrm{T}}\cdot\mathbf{V}\right) = \Psi\left(\mathbf{V}^2\right)\\ &= \Psi(\mathbf{b})\end{aligned} \tag{3.61}$$

known as Frame Indifference. Following so, the invariants with respect to $\mathbf{b}$ can be written as:

$$\mathrm{I}_1(\mathbf{b}) = \mathrm{I}_1(\mathbf{C}) \tag{3.62a}$$

$$\mathrm{I}_2(\mathbf{b}) = \mathrm{I}_2(\mathbf{C}) \tag{3.62b}$$

$$\mathrm{I}_3(\mathbf{b}) = \mathrm{I}_3(\mathbf{C}) \tag{3.62c}$$

Therefore, the derivatives used by equation 3.59 are also with respect to the invariants of $\mathbf{b}$ [18, 19, 20].

3.8.5 Transversely Isotropic Material

Composite materials or fibre-reinforced composites, are materials composed of a matrix material and one or more families of fibres. These types of materials are regarded as being heterogeneous, as their composition is different throughout the body, meaning that their mechanical response and properties are dependent on the direction, being named anisotropic materials [18].
A transversely isotropic material is a material that only has a single preferred direction, coincident to the fibre direction. The material response along orthogonal directions to the preferred direction is isotropic. A soft biological tissue can be regarded as one, as their composition can be approximated by collagen fibres and a substance matrix.

Considering that the anisotropic property of the material comes from the presence of fibres. For a material with only one family of fibres, the stress at a material point also depends on the fibre direction, as well as the deformation gradient. This direction at a

point $P \in \mathbf{B}_0$ (reference configuration), is defined by a unit vector field $\mathbf{a}_0(P)$, $|\mathbf{a}_0| = 1$. Subjected to deformation, the fibre adapts to a new direction in the current configuration,$\mathbf{B}_t$. This new fibre direction, now associated with point $Q \in \mathbf{B}_t$, is defined by a unit vector field, $\mathbf{a}(Q,t)$, $|\mathbf{a}| = 1$. The relation between the fibre direction in the reference and current configuration is given considering the length changes of the fibres. The stretch of the unit vector in the reference configuration, $\lambda_{\mathbf{a}_0}$ is possible to define with respect to the deformation gradient, as:

$$\lambda_{\mathbf{a}_0}(P,t) = \mathbf{F}\mathbf{a}_0 \tag{3.63}$$

The relationship between $\mathbf{a}_0$ and $\mathbf{a}$ is given by:

$$\lambda_{\mathbf{a}_0} = \lambda \mathbf{a} \tag{3.64}$$

Therefore, combining the two previous equations, it is possible to write the relation between fibre directions in both configurations, as:

$$\lambda \mathbf{a} = \mathbf{F}\mathbf{a}_0 \tag{3.65}$$

The material also shows a dependency on the direction, thus, the strain-energy function for a transversely isotropic material, will depend on both $\mathbf{C}$ (as seen previously for isotropic materials) and the fibre direction $\mathbf{a}_0$. Note that as the sense of $\mathbf{a}_0$ is immaterial, Ψ is taken as an even function of $\mathbf{a}_0$. As a result, Ψ is expressed as a function of the tensor product $\mathbf{a}_0 \otimes \mathbf{a}_0$. The strain-energy function for this type of material can be written as:

$$\Psi = \Psi\left(\mathbf{C}, \mathbf{a}_0 \otimes \mathbf{a}_0\right) \tag{3.66}$$

To describe the properties of the fibre family and its interaction with the other material constituents, two pseudo-invariants of $\mathbf{C}$ are defined, which are given by:

$$\mathrm{I}_4 = \mathbf{a}_0 \cdot \mathbf{C}\,\mathbf{a}_0 = \lambda^2 \tag{3.67a}$$

$$\mathrm{I}_5 = \mathbf{a}_0 \cdot \mathbf{C}^2 \mathbf{a}_0 \tag{3.67b}$$

The strain-energy function for a transversely isotropic material can now be finally defined as a function of five independent scalar invariants, according to:

$$\Psi = \Psi\left[\mathrm{I}_1(\mathbf{C}), \mathrm{I}_2(\mathbf{C}), \mathrm{I}_3(\mathbf{C}), \mathrm{I}_4\left(\mathbf{C}, \mathbf{a}_0\right), \mathrm{I}_5\left(\mathbf{C}, \mathbf{a}_0\right)\right] \tag{3.68}$$

As said previously, a transversely isotropic material can be described as being composed by a matrix material and a family or more of fibres, accordingly the total strain-energy function be divided into a contribution from the matrix,Ψ_{mat}, and a contribution from the

fibres,Ψ_{fib}, that can be written as:

$$\Psi = \Psi_{\text{mat}} + \sum^{i} \Psi_{\text{fib}_i} \tag{3.69}$$

where i is the number of family fibres.
Similarly to what was done for isotropic materials, the second Piola-Kirchhoff stress tensor $\mathbf{S}$ can be given as a function of the five invariants, as:

$$\mathbf{S} = \frac{\partial \Psi(\mathbf{C}, \mathbf{a}_0 \otimes \mathbf{a}_0)}{\partial \mathbf{C}} = 2 \sum_{i=1}^{5} \frac{\partial \Psi(\mathbf{C}, \mathbf{a}_0 \otimes \mathbf{a}_0)}{\partial \mathrm{I}_i} \frac{\partial \mathrm{I}_i}{\partial \mathbf{C}} \tag{3.70}$$

where the derivatives of the pseudo-invariants I_4 and I_5 are written as:

$$\frac{\partial \mathrm{I}_4}{\partial \mathbf{C}} = \mathbf{a}_0 \otimes \mathbf{a}_0 \tag{3.71a}$$

$$\frac{\partial \mathrm{I}_5}{\partial \mathbf{C}} = \mathbf{a}_0 \otimes \mathbf{C}\mathbf{a}_0 + \mathbf{a}_0 \mathbf{C} \otimes \mathbf{a}_0 \tag{3.71b}$$

which can then be substituted in equation 3.70 so that $\mathbf{S}$ can be given by:

$$\mathbf{S} = 2 \left[\left(\frac{\partial \Psi}{\partial \mathrm{I}_1} + \mathrm{I}_1 \frac{\partial \Psi}{\partial \mathrm{I}_2} \right) \mathbf{I} - \frac{\partial \Psi}{\partial \mathrm{I}_2} \mathbf{C} + \mathrm{I}_3 \frac{\partial \Psi}{\partial \mathrm{I}_3} \mathbf{C}^{-1} + \frac{\partial \Psi}{\partial \mathrm{I}_4} \mathbf{a}_0 \otimes \mathbf{a}_0 + \frac{\partial \Psi}{\partial \mathrm{I}_5} \left(\mathbf{a}_0 \otimes \mathbf{C}\mathbf{a}_0 + \mathbf{a}_0 \mathbf{C} \otimes \mathbf{a}_0 \right) \right] \tag{3.72}$$

Once again, the Cauchy stress tensor, $\boldsymbol{\sigma}$, referred to as the spatial counterpart of $\mathbf{S}$, can now be written for an transversely isotropic material, as [19]:

$$\boldsymbol{\sigma} = 2\, \mathrm{J}^{-1} \left[\left(\frac{\partial \Psi}{\partial \mathrm{I}_1} + \mathrm{I}_1 \frac{\partial \Psi}{\partial \mathrm{I}_2} \right) \mathbf{b} - \frac{\partial \Psi}{\partial \mathrm{I}_2} \mathbf{b}^2 + \mathrm{I}_3 \frac{\partial \Psi}{\partial \mathrm{I}_3} \mathbf{I} + \mathrm{I}_4 \frac{\partial \Psi}{\partial \mathrm{I}_4} \mathbf{a} \otimes \mathbf{a} + \mathrm{I}_4 \frac{\partial \Psi}{\partial \mathrm{I}_5} \left(\mathbf{a} \otimes \mathbf{b}\mathbf{a} + \mathbf{a}\mathbf{b} \otimes \mathbf{a} \right) \right] \tag{3.73}$$

3.9 Fibre Dispersion

The collagen fibres, referred to in section 3.8.5, within fibrous soft biological tissues, for instance, heart valves and in the case of the present work, the bladder wall, are responsible for their mechanical behaviour. The spatial variation orientation of the said fibres, more precisely their dispersion, has a significant effect on the mechanical response of the tissues [21]. Recent studies have shown that in the modelling of fibrous soft biological tissue, the dispersion of collagen fibres has a significant effect on the mechanical response compared when no dispersion is assumed [22].

3.9.1 Generalized Structure Tensor

The generalized structure tensor $\mathbf{H}$ allows directional data to be considered, so that distributed fibres as represented, developed by Gasser *et al.* [23].

Assuming the existence of a density function $\rho(\mathbf{N})$ where $\mathbf{N}\,(=\mathbf{a}_0)$ is the reference fibre orientation, the generalized structure tensor $\mathbf{H}$ is defined by,

$$\mathbf{H} = \frac{1}{4\pi}\int_{\mathbb{S}^2} \rho(\mathbf{N})\,\mathbf{N}\otimes\mathbf{N}\mathrm{d}\mathbb{S}^2 \tag{3.74}$$

with $\mathrm{tr}\mathbf{H} = 1$, and where $\mathbb{S}^2$ represents a unit sphere.

It is possible to characterize $\mathbf{N}$ in terms of two angles, figure 3.5, Θ and Φ, where, $\Theta \in [0,\pi]$ and $\Phi \in [0,2\pi]$ (Recall that as fibres are considered to be continuous, thus by symmetry the fibre i with orientation $\mathbf{N}_i$ is the same as a fibre with orientation $-\mathbf{N}_i$, hence the domain of Θ).

$$\mathbf{N} = \sin\Theta\cos\Phi e_1 + \sin\Theta\sin\Phi e_2 + \cos\Theta e_3 \tag{3.75}$$

where $\{e_1, e_2, e_3\}$ designates the axes of a rectangular Cartesian coordinate system.

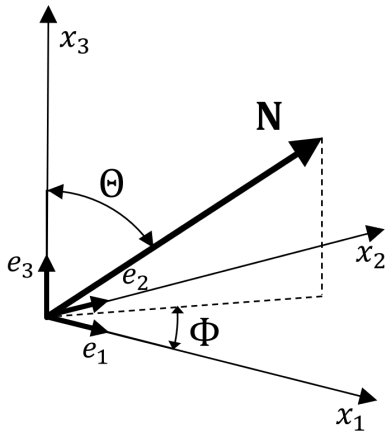

Figure 3.5: Characterization of an arbitrary fibre direction vector $\mathbf{N}$ by the means of Θ and Φ in a three-dimensional Cartesian coordinate system e_1, e_2, e_3.

Following this characterization, it is possible to rewrite the generalized structure tensor $\mathbf{H}$ in a compact form,

$$\mathbf{H} = \sum_i^3 \sum_j^3 \alpha_{ij} e_i \otimes e_j \tag{3.76}$$

where the coefficients α_{ij} are defined by:

$$\alpha_{11} = \frac{1}{4\pi}\int_{S^2} \rho(\mathbf{N}) \sin^3\Theta \cos^2\Phi \mathrm{d}\Theta\mathrm{d}\Phi \tag{3.77a}$$

$$\alpha_{22} = \frac{1}{4\pi}\int_{S^2} \rho(\mathbf{N}) \sin^3\Theta \sin^2\Phi \mathrm{d}\Theta\mathrm{d}\Phi \tag{3.77b}$$

$$\alpha_{33} = \frac{1}{4\pi}\int_{S^2} \rho(\mathbf{N}) \cos^2\Theta \sin\Phi \mathrm{d}\Theta\mathrm{d}\Phi \tag{3.77c}$$

$$\alpha_{12} = \alpha_{21} = \frac{1}{4\pi}\int_{S^2} \rho(\mathbf{N}) \sin^3\Theta \sin\Phi \cos\Phi \mathrm{d}\Theta\mathrm{d}\Phi \tag{3.77d}$$

$$\alpha_{23} = \alpha_{32} = \frac{1}{4\pi}\int_{S^2} \rho(\mathbf{N}) \sin^2\Theta \cos\Theta \sin\Phi \mathrm{d}\Theta\mathrm{d}\Phi \tag{3.77e}$$

$$\alpha_{13} = \alpha_{31} = \frac{1}{4\pi}\int_{S^2} \rho(\mathbf{N}) \sin^2\Theta \cos\Theta \cos\Phi \mathrm{d}\Theta\mathrm{d}\Phi \tag{3.77f}$$

For a transversely isotropic material, a given family of fibres, with direction $\mathbf{a}_0$, are distributed with symmetry around a mean referential direction. Consider the fibre direction $\mathbf{a}_0$ to be coincident with e_3, the density function ρ is now, on this particular case, independent of Φ, $\rho(\Theta, \Phi) \rightarrow \rho(\Theta)$. Accordingly, the off-diagonal coefficients of $\mathbf{H}$, equation 3.77 ($i \neq j$) are zero. While the diagonal terms are given by,

$$\alpha_{11} = \alpha_{22} = k \quad \wedge \quad \alpha_{33} = 1 - 2k \tag{3.78}$$

where k is introduced as a dispersion parameter and equal to:

$$k = \frac{1}{4}\int_0^{\pi} \rho(\Theta) \sin^3\Theta \mathrm{d}\Theta \tag{3.79}$$

The values of k are between $[0, 1/3]$ where $k = 0$ means that there is no dispersion and $k = 1/3$ corresponds to a three-dimensional isotropic distribution of fibres orientations, as explained in more detail by Holzapfel & Ogden [24].

Consequently, the generalized structure tensor $\mathbf{H}$ can finally be given in the compact form by

$$\mathbf{H} = k\mathbf{I} + (1 - 3k)\,\mathbf{a}_0 \otimes \mathbf{a}_0 \tag{3.80}$$

where $\mathbf{I}$ is the identity tensor.

The generalized structure tensor $\mathbf{H}$ approach is responsible for the development of the GHO constitutive model, that will be explored in chapter 4.

The limitation of this approach is the restriction it implies. See that equation 3.80, that defines the compact form $\mathbf{H}$ and lead to the development of a constitutive model, is only suited for transversely isotropic materials, where the fibres are considered continuous and distributed with symmetry around a mean referential direction. Therefore, the angular integration approach enables to use any fibre distribution density function with direct application in the constitutive model.

3.9.2 Angular Integration

Considering a typical fibre, in the reference configuration, that has an orientation $\mathbf{N}$. The orientation of the fibre is taken into consideration by strain-energy function, Ψ, by the means of the pseudo-invariants, I_4 and I_5, of $\mathbf{C}$. The issue with this more simplistic approach is that it considers the fibres to be locally aligned. Angular integration (AI) considers a more realistic situation, regarding the fibres, that acknowledges a distribution of orientations [21].

In the AI approach, the strain-energy of a single fibre is considered a function of the fibre stretch, $\Psi_{\text{fib}}(\lambda_{\text{f}})$, introduced by Lanir in [25]. The fibre dispersion in the tissue is assimilated into the strain-energy by an integration of a single fibre strain-energy over all fibres directions weighted with a probability density function. By doing so, the total strain-energy function associated with the fibre contribution, Ψ_{AI}, is obtained by integrating the weighted strain energy, $\Psi_{\text{fib}}(\lambda_{\text{f}})$ (as presented in 3.8.5), for each fibre direction $\mathbf{N}$ over a unit sphere $\mathbb{S}^2$ [26], it is written as:

$$\Psi_{\text{AI}} = \frac{1}{4\pi} \int_{\mathbb{S}^2} \rho(\mathbf{N})\, \Psi_{\text{fib}}(\lambda_{\text{f}})\, \mathrm{d}\mathbb{S}^2 \tag{3.81}$$

where $\rho(\mathbf{N})$ represents the probability density of the fibre in that direction in the reference configuration, and should be determined by imaging analysis. In the singular case where no dispersion if found, $\Psi_{\text{AI}} = \Psi_{\text{fib}}$. Thus, the factor $1/4\pi$ is used to promote this parity. The probability density function is normalized according to,

$$\frac{1}{4\pi} \int_{\mathbb{S}^2} \rho(\mathbf{N})\, \mathrm{d}\mathbb{S}^2 = 1 \tag{3.82}$$

Assuming a 3D dispersion of the fibres inside the matrix material, the probability function $\rho(\mathbf{N})$ can be written as $\rho(\Theta, \Phi)$, defined over the unit sphere $\mathbb{S}^2$,

$$\mathbb{S}^2 = \{(\Theta, \Phi) \mid \Theta \in [0, \pi], \Phi \in [0, 2\pi]\} \tag{3.83}$$

Equation 3.81 can be written as,

$$\Psi_{\text{AI}} = \frac{1}{4\pi} \int_0^{2\pi} \int_0^{\pi} \rho(\Theta, \Phi)\, \Psi_{\text{fib}}(\lambda_{\text{f}}) \sin(\Theta)\, \mathrm{d}\Theta \mathrm{d}\Phi \tag{3.84}$$

Due to the complex nature of the strain-energy function of the fibres and the probability density, $\rho(\mathbf{N})$ now $\rho(\Theta, \Phi)$ and Ψ_{fib} respectively. Analytical solutions of equation 3.81 only exist for some cases. The more frequent approach is to evaluate the integral that defines Ψ_{AI}, by numerical methods such as,

$$\Psi_{\text{AI}} \approx \frac{1}{4\pi} \sum_{n=1}^{m} \rho(\Theta, \Phi)\, \Psi_{\text{fib}}(\lambda_{\text{f}_n})\, w_n \tag{3.85}$$

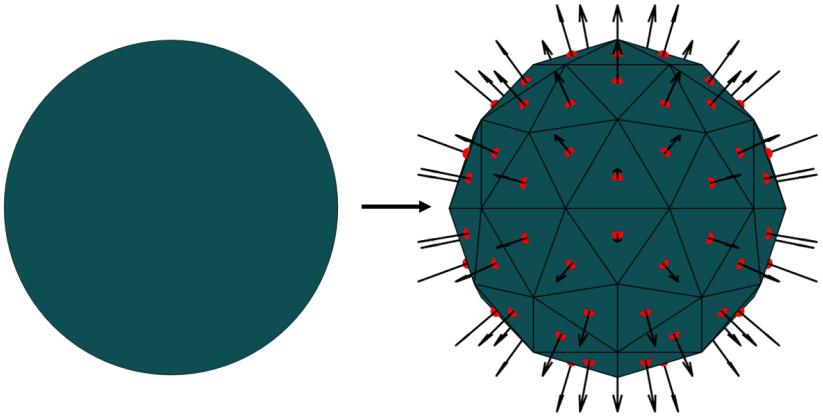

(a) $m = 80$.

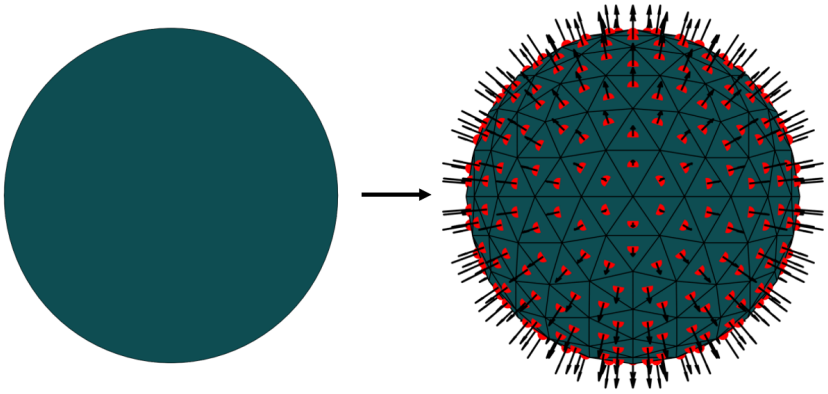

(b) $m = 320$.

Figure 3.6: Representation of a discretization defined over a unit sphere $\mathbb{S}^2$ with the each centroid (marked in red) angle pair direction (marked by an arrow).

where $(\Theta, \Phi) \equiv \mathbf{N}_n$ and w_n are, for $n = 1, ..., m$ integration points (representative of orientations) and weights defined by the integration scheme over the unit sphere, m is the number of integration points, and λ_{f_n} are the stretches associated with the integration points.

The first step is to discretize the unit sphere, $\mathbb{S}^2$ into a finite number of elementary areas, in this case spherical triangles, $\Delta\mathbb{S}^2_n$, $n = 1, ..., m$. Then, the centroid of each spherical triangle $\Delta\mathbb{S}^2_n$, $n = 1, ..., m$ is associated with a angle pair (Θ_n, Φ_n) representative of a fibre direction. This process is represented in figure 3.6, where in 3.6a the number of areas m from equation 3.85 is 80 and in 3.6b $m = 320$ [21, 26].

Chapter 4

Proposed Bladder Constitutive Equation

4.1 Bladder Behaviour

The bladder is a highly compliant organ, continually subjected to large deformations throughout the micturition cycle. The histology (or microstructure) of the bladder wall needs to be taken into consideration when modeling the organ. From chapter 2 recall that the bladder wall when empty, exhibit numerous folds and the collagen fibres, within the submucosa layer, are crimped. These characteristics provide a mechanism for low resistance flattening without any discernible recruitment of collagen fibres, explaining the high compliance of the bladder, as the initial part of the bladder wall deformation is accomplished without any fibre contribution [27, 3].

4.1.1 Fibre Recruitment

The arrangement and morphology of collagen fibres within the bladder wall exhibit a certain degree of waviness, as they are crimped. Fibre recruitment is inherently connected the the degree of waviness, the higher degree the higher fibre recruitment. The fibre only starts to contribute to the strain-energy function of the tissue once it is straightened, before that, the straightening of fibres from a wavy state to a straightened state involves no stress contribution [28].

The behaviour can be modelled by defining a normalized true fibre stretch as

$$\lambda_n = \frac{\lambda_f}{\lambda_r} \tag{4.1}$$

Where $\lambda_f = \sqrt{\mathbf{N}^T \cdot \mathbf{CN}}$ denotes the fibre stretch if there is no recruitment, and λ_r defines the fibre recruitment stretch, a material property, at which the fibres becomes straightened, note that for $\lambda_f \leq \lambda_r$ the fibre has no contribution to the strain energy function [29].

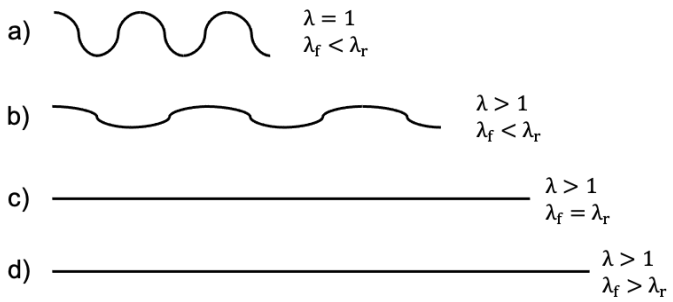

Figure 4.1: Deformation of a single collagen fibre regarding fibre recruitment state.

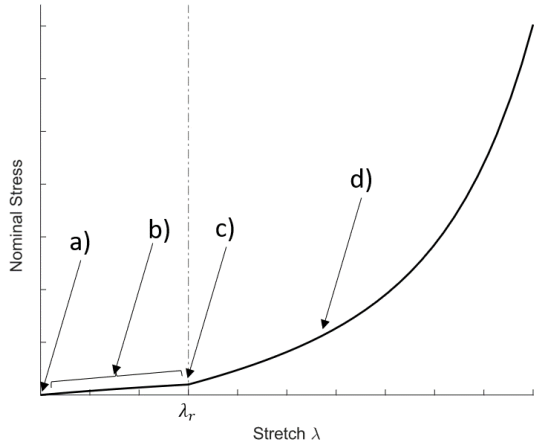

Figure 4.2: Nominal stress response regarding fibre recruitment state.

See figure 4.1 and 4.2. Situation (a), the initial state, refers to the moment the bladder is found empty. The current fibre stretch λ_f is 1.0 equal to the stretch of the tissue λ. As the starts to fill $\lambda > 1$, the fibre begins to straighten, situation (b), where $1 < \lambda_f < \lambda_r$, during which there is no stress contribution from the fibres. After the straightening of the fibre, situation (c), there is a stage where $\lambda_f = \lambda_r$. Subsequently, $\lambda_f > \lambda_r$, situation (d), and the fibre starts to contribute to the strain-energy function [28].

In 3.8.5 was introduced a division on the strain-energy function, regarding the contribution of the material and the family of fibres. Recall equation 3.69 for one family of fibres,

$$\Psi = \Psi_{mat} + \Psi_{fib} \tag{4.2}$$

where Ψ_{mat} refers to the contribution of the matrix material and Ψ_{fib} refers to the contribution of a fibre. Ψ_{fib} needs to be redefined to account for fibre recruitment. Accordingly,

the strain-energy function can be given as:

$$\Psi = \Psi_{\text{mat}} + f\Psi_{\text{fib}} \tag{4.3}$$

where Ψ_{fib} is now given in terms of the normalized stretch λ_{n}, and f function as a switch, to evaluate the fibre recruitment, defined as:

$$f = \begin{cases} 1 & \lambda_{\text{f}} > \lambda_{\text{r}} \\ 0 & otherwise \end{cases} \tag{4.4}$$

4.2 Forms of Strain-Energy Function

The response to deformation of hyperelastic materials is traduced by a strain-energy function, Ψ. Over the years, numerous specific forms of strain-energy functions have been proposed aiming to describe the behaviour of each material, regarded to as material models. During this section, material models that better suit the scope of this work will be presented, which are well tried within the constitutive theory and frequently employed in the literature [19].

4.2.1 Neo-Hookean Model

Proposed in 1943, the Neo-Hookean model, derived from molecular chain statistics theory, is given by:

$$\Psi = \text{C}_{10}\left(\text{I}_1 - 3\right) \tag{4.5}$$

where I_1 is the first invariant of $\mathbf{C}$ given by equation 3.55a. This model involves a single parameter, C_{10} related to the shear modulus as $\text{C}_{10} = \mu/2$, and provides a simple and reliable constitutive model for the deformation behaviour of isotropic rubber-like materials [19, 30].

4.2.2 Ogden Model

Proposed in 1972, the Ogden model is a very sophisticated approach to simulate incompressible rubber-like materials [31]. The strain-energy function depends on the principal stretches, $\lambda_{1,2,3}$ as it describes their changes from the reference to current configuration, and can be written as,

$$\Psi = \Psi\left(\lambda_1, \lambda_2, \lambda_3\right) = \sum_{p=1}^{N} \frac{\mu_p}{\alpha_p}\left(\lambda_1^{\alpha_p} + \lambda_2^{\alpha_p} + \lambda_3^{\alpha_p}\right) \tag{4.6}$$

where N is a positive integer that translates the number of terms in the strain-energy function. μ_p are pseudo shear moduli and α_p dimensionless parameters. Regarding linear

theory, it is possible to write:

$$2\mu = \sum_{p=1}^{N} \mu_p \alpha_p \quad \text{with} \quad \mu_p \alpha_p > 0 \quad \text{for} \quad p = 1, ..., N \tag{4.7}$$

known as the consistency condition. It is possible, therefore, obtain the relation between the model parameters [19, 30, 31]. This model exhibits a good behaviour when dealing the high compliant materials, however, it lacks the ability to describe the microstructure of materials, such as the presence of fibres. Another characteristic of this model is that it is written in terms of the principal stretches, whereas normally the models are defined in terms of the invariants of the Cauchy-Green deformation tensors.

4.2.3 Holzapfel-Gasser-Ogden Model

Proposed in 2000, the Holzapfel-Gasser-Ogden (HGO) was developed to provide a constitutive relation for the passive response of arterial walls [32]. For the contribution of the isotropic matrix, the HGO model considers the Neo-Hookean model. The fibre contribution from the fibre i of P fibre families, Ψ_{fib_i} the HGO model assumes:

$$\Psi_{\text{fib}_i} = \frac{k_{1_i}}{2k_{2_i}} \left[e^{k_{2_i}\left(\text{I}_{4_i}-1\right)^2} - 1 \right] \tag{4.8}$$

where k_{1_i} is a stress like parameter and k_{2_i} is a dimensionless parameter of the i^{th} family of fibres.

Following so, the HGO model is finally given by:

$$\Psi = \Psi_{\text{mat}} + \Psi_{\text{fib}} = \text{C}_{10}\left(\text{I}_1 - 3\right) + \sum_{i=1}^{P} \frac{k_{1_i}}{2k_{2_i}} \left[e^{k_{2_i}\left(\text{I}_{4_i}-1\right)^2} - 1 \right] \tag{4.9}$$

4.2.4 Gasser-Holzapfel-Ogden Model

Recall from section 3.9.1, equation 3.80 defined the generalized structure tensor $\mathbf{H}$ as,

$$\mathbf{H} = k\mathbf{I} + (1 - 3k)\, \mathbf{a}_0 \otimes \mathbf{a}_0 \tag{4.10}$$

Proposed in 2006 by Gasser *et al.* in [23], Gasser-Holzapfel-Ogden (GHO) model defines the fibre contribution of the i^{th} family of collagen fibres Ψ_{fib_i} in the form of:

$$\Psi_{\text{fib}_i} = \frac{k_{1_i}}{2k_{2_i}} \left[e^{k_{2_i} E_i^2} - 1 \right] \tag{4.11}$$

where, $E_i = \mathbf{H}_i : \mathbf{C} - 1$ and $\mathbf{H}_i = k\mathbf{I} + (1 - 3k)\, \mathbf{a}_{0_i} \otimes \mathbf{a}_{0_i}$.

If, I_{4i} is rewritten as, $\mathrm{I}_{4i} = \mathbf{a}_{0_i} \otimes \mathbf{a}_{0_i} : \mathbf{C}$, then E_i can be given as $E_i = k\mathrm{I}_1 + (1-3k)\,\mathrm{I}_{4i} - 1$, the fibre contribution from the GHO model, can finally be given by:

$$\Psi_{\mathrm{fib}_i} = \frac{k_{1_i}}{2k_{2_i}} \left[e^{k_{2_i}\left[k\mathrm{I}_1 + (1-3k)\mathrm{I}_{4_i} - 1\right]^2} - 1 \right] \tag{4.12}$$

The most fundamental difference between the HGO and GHO model is that the latter, the fibre contribution depends on the first invariant of $\mathbf{C}$, I_1. The matrix contribution to the strain-energy function Ψ_{mat} on the GHO model is given by the NH model [23].

4.3 Proposed Model

Two commonly employed methods for modelling the mechanical behaviour of soft tissues are a phenomenological and a microstructural approach. Phenomenological constitutive relations are formulated primarily based to fit data. The major advantage of this approach is that the result is a simple mathematical relation. However, the disadvantage of this method is the exclusivity of the results, meaning that it does not account for load-dependent behaviour exhibited by many tissues. As an example, a relation based on such approach is incapable to describe the behaviour of a tissue under changing load or material reorientation. From a microstuctural perspective, it attempts to describe the mechanical behaviour, geometry, and interactions between the individual constituents comprising the tissue. However, mathematically more complex, this approach enables constitutive models to characterize load-dependent responses [33, 34, 35].

Bladder wall tissue is composed of, among other constituents, muscle, collagen, and elastin fibres, distributed in different layers, see chapter 2. Regarding the fibre direction, it is possible to identify two groups of fibres with distinct directions. A longitudinal orientation, where the fibres run from apex to base, and a circular orientation. Both orientations are transverse in relation to one another. Therefore, it is possible to consider that the tissue is composed of two dominant fibres systems (composed of muscle and collagen fibres) and a gel-like matrix. Accordingly, a pseudostrain-energy function capable of describing the behaviour of the bladder would have the form of:

$$\Psi = \Psi_{\mathrm{mat}} + \sum_{i=1}^{2} \Psi_{\mathrm{fib}_i} \tag{4.13}$$

where Ψ_{mat} and Ψ_{fib_i} represent the energy stored in the matrix and in the two family fibres, respectively.

A family of fibres is defined as locally aligned, however, seen in section 3.9, the spatial variation of the fibres has a significant effect on the mechanical response of the tissue. Thereupon, it is beneficial to model the dispersion of fibres. Following an angular integration (AI) approach, it is possible to rewrite as pseudostrain-energy function to model

the bladder wall response as,

$$\Psi = \Psi_{\text{mat}} + \frac{1}{4\pi}\sum_{i=1}^{2}\int_{\mathbb{S}^2}\rho_i(\mathbf{N})\,\Psi_{\text{fib}_i}\mathrm{d}\mathbb{S}^2 \tag{4.14}$$

where $\rho_i(\mathbf{N})$ represents the probability density of the i^{th} family of fibres.

One way to approach the modelling of the bladder wall would be to consider the HGO model, 4.2.3, in combination with AI, that would result in:

$$\Psi = \mathrm{C}_{10}\left(\mathrm{I}_1 - 3\right) + \frac{1}{4\pi}\sum_{i=1}^{2}\int_{\mathbb{S}^2}\rho_i(\mathbf{N})\,\frac{k_{1_i}}{2k_{2_i}}\left[e^{k_{2_i}\left(\mathrm{I}_{4_\mathrm{i}}-1\right)^2}-1\right]\mathrm{d}\mathbb{S}^2 \tag{4.15}$$

There are two considerations that need to be taken regarding this approach. The morphology of the collagen fibres is not being taken into account. Recall that at an initial state, there is no stress contribution from the fibres, the contribution only starts when the fibre is straightened. In order to account for fibre recruitment, two steps need to be followed. First, the switch f from equation 4.4 needs to be applied to the fibre contribution part of the pseudostrain-energy function. Second, the pseudo-invariant of I_4 need to be reevaluated as a normalized pseudo-invariant $\mathrm{I}_{4\mathrm{n}}$ regarding the recruitment stretch λ_r. Remember equation 3.67a and $\lambda_\mathrm{f} = \sqrt{\mathbf{N}^T\cdot\mathbf{CN}}$, a relation can be given by:

$$\mathrm{I}_4 = \mathbf{N}^T\cdot\mathbf{CN} = \lambda_\mathrm{f}^2 \tag{4.16}$$

Hence, the normalized pseudo-invariant $\mathrm{I}_{4\mathrm{n}}$ can be given by,

$$\mathrm{I}_{4\mathrm{n}} = \left(\frac{\lambda_\mathrm{f}}{\lambda_\mathrm{r}}\right)^2 \tag{4.17}$$

Accordingly, regarding fibre recruitment, the pseudostrain-energy function could be given as:

$$\Psi = \mathrm{C}_{10}\left(\mathrm{I}_1 - 3\right) + f\frac{1}{4\pi}\sum_{i=1}^{2}\int_{\mathbb{S}^2}\rho_i(\mathbf{N})\,\frac{k_{1_i}}{2k_{2_i}}\left[e^{k_{2_i}\left(\mathrm{I}_{4\mathrm{n}_\mathrm{i}}-1\right)^2}-1\right]\mathrm{d}\mathbb{S}^2 \quad \text{with} \quad f = \begin{cases}1 & \lambda_\mathrm{f} > \lambda_\mathrm{r}\\ 0 & \textit{otherwise}\end{cases} \tag{4.18}$$

The other consideration to make is regarding the bladder compliance. As previously mentioned, the bladder is a highly compliant organ due to its microstructure. Being subjected to large deformations, without a direct translation to the response regarding the stress, meaning that the stress response is not proportional to the deformation, when compared to other organs. As the HGO model was developed with the aim to describe arterial walls, its current form is not suited to characterize the behaviour of the bladder, since arterial walls exhibit a much higher stiffness. Therefore, there was a need to change the behaviour of pseudostrain-energy function Ψ, equation 4.18, in relation to the tissue

stretch λ. The dependency on λ arrives from the normalized pseudo-invariant I_{4n} as:

$$I_{4n} = \left(\frac{\lambda_f}{\lambda_r}\right)^2 = \left(\frac{\sqrt{\mathbf{N}^T \cdot \mathbf{C}(\lambda)\,\mathbf{N}}}{\lambda_r}\right)^2 \tag{4.19}$$

Several approaches were considered and the one to provide a better approximation to the bladder wall behaviour was the following. If instead of the normalized pseudo-invariant I_{4n} the pseudostrain-energy function used its square root, as, $\Psi(I_{4n}) \Rightarrow \Psi\left(\sqrt{I_{4n}}\right)$, the order on which λ is accounted for by the constitutive model, is reduced by half. Note that I_{4n} is a dimensionless, so the proposed change has no direct influence on the units of the pseudostrain-energy function parameters.

Figures 4.3a and 4.3b show a direct comparison, with a random set o parameters and material properties, between the pseudostrain-energy function considering the HGO model and considering the proposed model with square rooted normalized pseudo-invariant. As the bladder wall can subjected to large deformations, $\lambda_{max} \geq 3$, figure 4.3a shows the exponential behaviour of the model, unsuited for this range of stretches. Figure 4.3b shows a smaller range of stretch, were it is possible to observe the response difference between both approaches in relation to the deformation, as stretch. Note on figure 4.3b that before the fibre recruitment begins, $\lambda \leq \lambda_r$, the response of both models was the same. This is expected as the strain-energy function of the matrix is the same in both approaches, remembering that if $\lambda \leq \lambda_r \Rightarrow \Psi = \Psi_{mat}$.

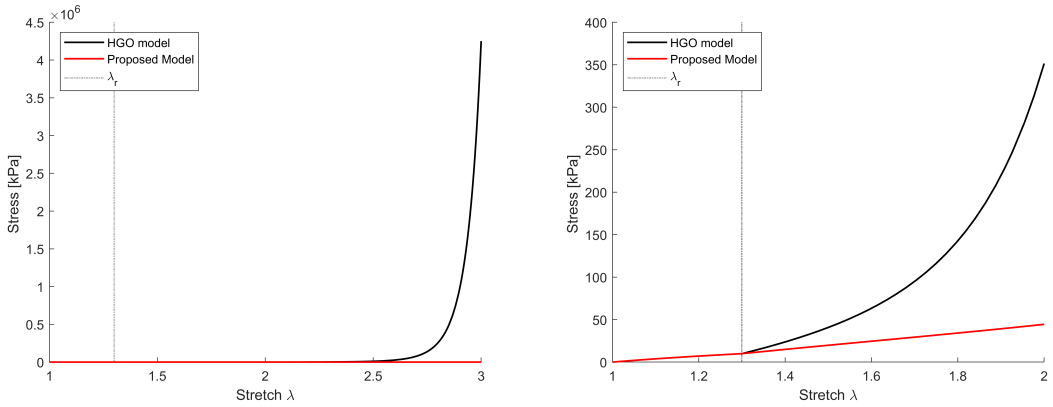

(a) $\lambda \in [1, 3]$. (b) $\lambda \in [1, 2]$.

Figure 4.3: Comparison between HGO based model and proposed model.

Finally, the proposed pseudostrain-energy function to describe the behaviour of the bladder wall, considering fibre recruitment and dispersion of fibres, following an angular

integration approach, is written as:

$$\Psi = C_{10}\,(I_1 - 3) + \frac{1}{4\pi}\sum_{i=1}^{2}\int_{\mathbb{S}^2} f_i \rho_i(\mathbf{N})\,\frac{k_{1_i}}{2k_{2_i}}\left[e^{k_{2_i}\left(\sqrt{I_{4_{n_i}}}-1\right)^2} - 1\right] d\mathbb{S}^2 \quad \text{with} \quad f_i = \begin{cases} 1 & \lambda_{f_i} > \lambda_{r_i} \\ 0 & otherwise \end{cases} \tag{4.20}$$

The derivatives and definition of the Cauchy stress tensor considering the new proposed model can be found in appendix A.

4.3.1 Discussion & Model Fitting

The aim of the proposed model was to describe the behaviour of the bladder wall, taking into consideration its microstructure and characteristics. That means being able to account for fibre recruitment, fibre dispersion and the high compliance of the bladder wall. The fibre recruitment was addressed by normalizing the pseudo-invariant I_4 and using a switch f to account only for fibres under tension. The dispersion of the fibres was tackled by the means of angular integration, where a distribution of orientations is considered. Finally, the bladder compliance was regarded by reducing the order on which the stretch is considered in the pseudostrain-energy function $\lambda \leq \lambda_r \Rightarrow \Psi = \Psi_{mat}$.

The applicability of the proposed strain-energy function is tested and verified by comparison with experimental results from bladder tissue testing. Accordingly, the proposed model, equation 4.20, was fitted to experimental results found in the literature. Maryam Sami Jokandan *et al.* in [2] performed uniaxial tests on a female porcine bladder, obtained the results (in the longitudinal direction) in figure 4.4.

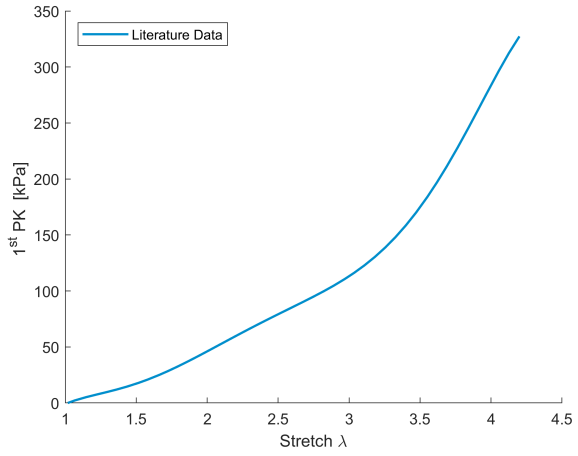

Figure 4.4: Experimental uniaxial tests results on a female porcine bladder from [2].

4.3.1.1 Model Fitting Procedure

In order to fit the proposed model to experimental results, the parameters and material properties on which the model is based need to be determined and assigned. All fittings

conducted during this work were manually done, in order to keep a better control on the parameters values, afterwards an optimization algorithm could be used to promote an even better fit. Data from figure 4.4 is from uniaxial tests done to assess the longitudinal fibres/direction, thus, the proposed model from equation 4.20 can be used with only one family of fibres. As it is defined, the proposed model, equation 4.20, for one family of fibres depends on C_{10}, k_1, k_2, $\rho(\mathbf{N})$, and λ_r.

The probability density function (PDF) $\rho(\mathbf{N})$ should, ideally, be determined by imaging analyses from second harmonic generation, as the function can be applicable to any type of fibre dispersion [26]. In the context of this work, the fibres are considered to be continuous and rotationally symmetric, so it was chosen a von Mises distribution following what was proposed in [26],

$$\rho(\mathbf{N}) = 4\sqrt{\frac{b}{2\pi}}\frac{exp\left[2b\left(\mathbf{N}\cdot\mathbf{M}\right)^2\right]}{erfi\left(\sqrt{2b}\right)} \tag{4.21}$$

where b is a concentration parameter, describing how closely the fibres are distributed around the mean fibre direction $\mathbf{M}$, and $erfi\left(x\right) = -\mathrm{i}\,erf\left(\mathrm{i}x\right)$ denotes the imaginary error function and $erf\left(x\right)$ is the standard error function. However fibre dispersion was only considered in the numerical simulation, chapter 6. The next figures, where experimental data was fitted to the model, did not consider dispersion. The MATLAB script used can be found in appendix B.

The determination of the fibre recruitment stretch λ_r should be from image analyses not only of the fiber morphology of the specimen and but also deformed fibres. However, due to the lack of these data, it can be approximated from the stress vs stretch curves by determining the stretch level at which the slope of the curve starts to increase as a consequence of the fibre contribution, figure 4.5a [28].

The remaining parameters are determined by analysing the curve. Note that, C_{10} influence is most noted before the fibre recruitment stretch, figure 4.5b. The region right after the fibres start to be recruited, the response is mostly controlled by k_1, figure 4.5c. Finally, the exponential growth of the model is controlled by k_2, figure 4.5c.

Accordingly, the procedure is represented in figure 4.5, after the concentration parameter b is set, is done from left to right, following the stretch λ, following the figures 4.5a $\rightarrow$ 4.5b $\rightarrow$ 4.5c $\rightarrow$ 4.5d.

Martins *et al.* in [36] performed uniaxial tests of human bladder, with tissue samples were obtained from 13 female cadavers without pelvic floor dysfunctions. In figure 4.6, it is shown the new proposed model fitted with the results from the conducted tests.

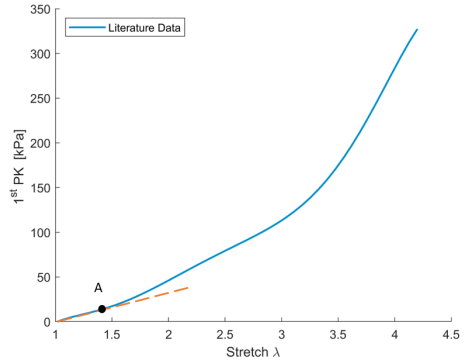

(a) Estimated λ_r, point A.

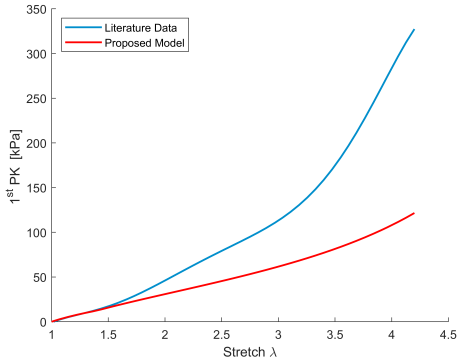

(b) $\lambda_r = 1.4 | C_{10} = 7\text{kPa} | k_1 = 20\text{kPa} | k_2 = 0.20$

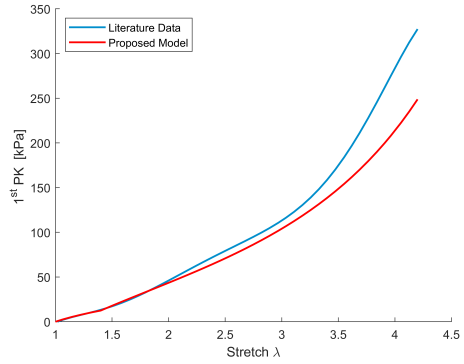

(c) $\lambda_r = 1.4 | C_{10} = 7\text{kPa} | k_1 = 60\text{kPa} | k_2 = 0.20$

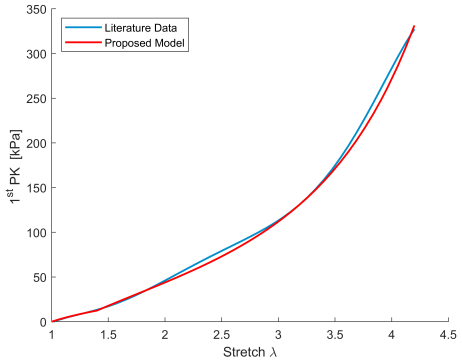

(d) $\lambda_r = 1.4 | C_{10} = 7\text{kPa} | k_1 = 60\text{kPa} | k_2 = 0.29$

Figure 4.5: Model fitting procedure with experimental curves.

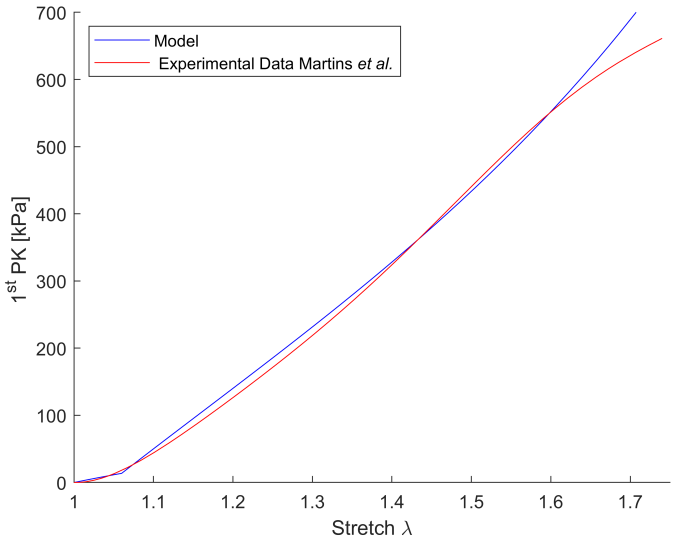

Figure 4.6: Model fitting with experimental uniaxial tests results of human female bladder from [36], where $\lambda_r = 1.06 \mid C_{10} = 40\,\text{kPa} \mid k_1 = 790\,\text{kPa} \mid k_2 = 0.70$

Chapter 5

Experimental Testing

5.1 Sample Preparation

During the development of this work, experimental testing were conducted. The results from said tests will serve as a basis for the upcoming chapter as the properties of the bladder wall will be determined to fit the experimental data. Bladder tissue was collected from a female porcine, cleaned and stored in a freezer before being slowly defrosted ($>$ 24h) before any preparation work began. The samples were cutted, using surgical scissors and scalpel, and prepared to enable the assessment of both longitudinal and circular fibres. The samples were kept hydrated with saline solution. The sample layout within the bladder can be seen in figure 5.1.

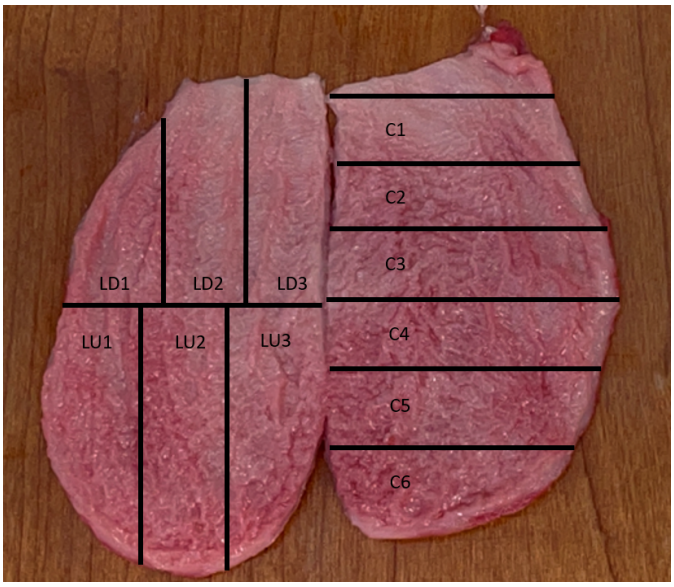

Figure 5.1: Sample layout.

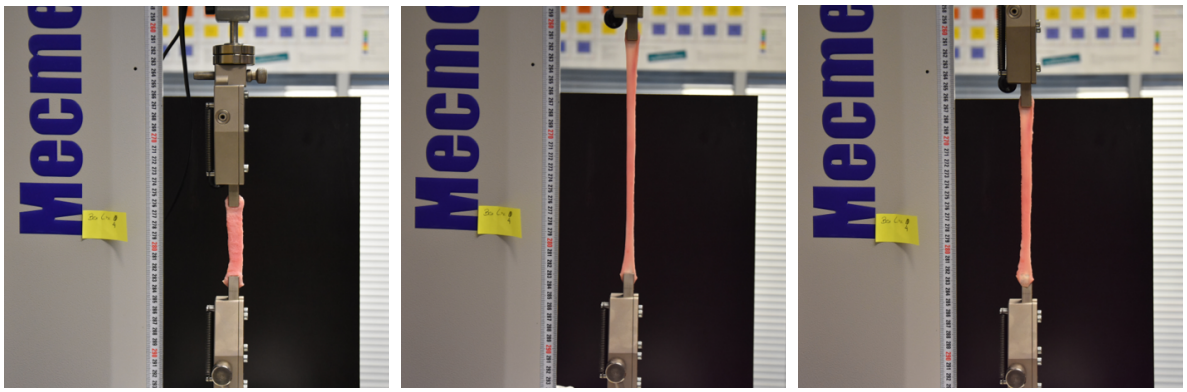

(a) (b) (c)

Figure 5.2: (a) Sample positioning | (b) Sample elongation | (c) Sample permanent deformation.

The initial length of each sample, as well as the width were acquired through digital image analyses, taken with a camera after a preconditioning of 0.04 N, that served as a reference for zero-displacement point. The thickness was measured with a caliper after the sample placement, at three different points and the average was taken and considered. The load and displacement data were acquired using a Mecmesin AFG 100N load cell and processed with Vector Pro (version 2.1.0.0). Following the placement and measuring of the sample, the uniaxial test began with a constant velocity of 10 mm/min (as used in [2]) as a slower speed would result in a unwanted drying of the tissue. Figure 5.2a shows one of the tested samples before the solicitation began. Next figure, figure 5.2b shows the same sample near the end of the test, while figure 5.2c shows the permanent deformation of the tissue.

5.2 Experimental Results

As all the samples were tested, the data collected (extension $l\,[mm]$ vs force $F\,[\mathrm{N}]$) was exported. Figure 5.3a shows the results from all the samples tested during this work. For convenience and parity with continuum mechanics, the extension l was transformed in stretch λ with relation to the initial lenght of each sample l_0, given by:

$$\lambda = \frac{l + l_0}{l_0} \tag{5.1}$$

On the other hand, the force F was transformed into the 1st PK stress tensor $\mathbf{P}$ by dividing it by the initial (reference) area a_0, as:

$$\mathbf{P} = \frac{F}{a_0} \tag{5.2}$$

The $\mathbf{P}$ vs λ curves are now presented in figure 5.3b.

Analyzing the experimental results, see figure 5.3b, it is found that three of the samples (C1, C2 and C6) results lay outside the expected behaviour. The first two samples, C1 and C2, were the first to be tested, and during the test the sample slipped from clamps, causing the test to be stopped and restarted, causing in a undesired change in results. During the last of the samples tested to asses the circular fibres, C6, there was a problem with the data acquisition software, resulting in missing data. Therefore, the results from these three samples were ignored for the remaining part of this work. In the context of this work, the most important region of study is where the elastic behaviour of the tissue is observed. Accordingly, the domain of stretch analysed was reduced to $\lambda \in [0, 3]$ to represent the region of interest.

With the remaining curves, and respective computed regression, the results where converted into not only the average of the circular and longitudinal fibres, but also the total average, figure 5.3c.

To assess the differences between circular and longitudinal fibres, the standard deviation of each set of samples was calculated, figure 5.3d. Regardless of the similarity between both curves, it was considered that treating the fibres as different would be a better approach in the context of this work, as the standard deviation proved to be possible to differentiate them.

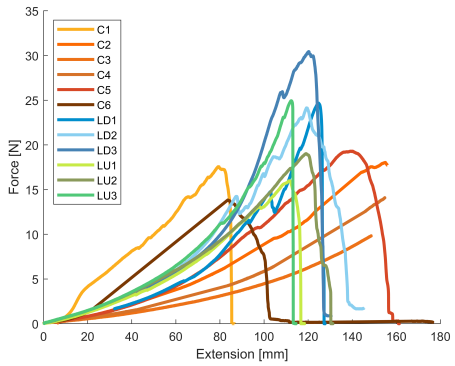

(a) Force vs extension.

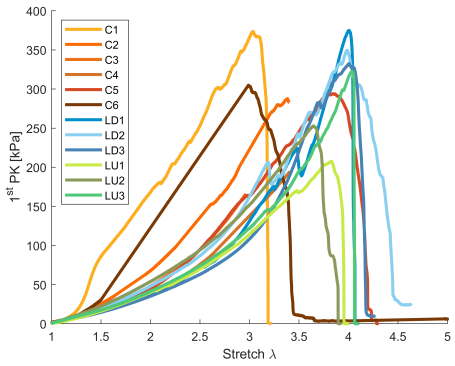

(b) 1st PK vs stretch.

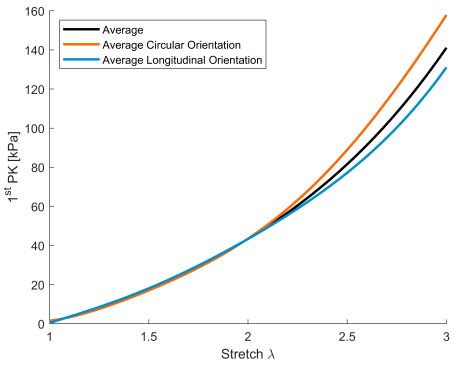

(c) Average.

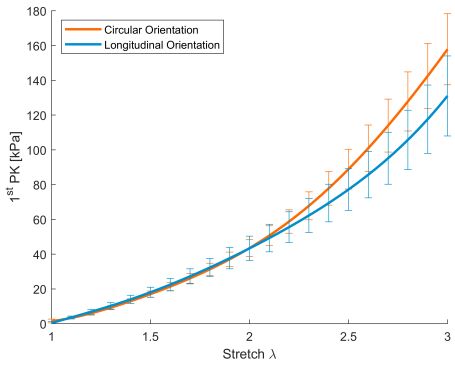

(d) Average and standard deviation.

Figure 5.3: Experimental results curves.

5.3 Data Validation

In order to validate the experimental results, a comparison was made with published studies. Maryam Sami Jokandan *et al.* in [2] performed uniaxial tests on a female porcine bladder. The conditions of these tests were similar to the ones during this work. The samples were loaded at $10\,mm/min$ with a preconditioning of $0.05\,N$ (vs $0.04\,N$ on this work). The study also made a distinction between longitudinal and circular directions.

The graph in figure 5.4 shows a direct comparison between longitudinal fibres/direction. In blue, the results from this work and in black, the published results from the uniaxial test conducted by Maryam Sami Jokandan *et al.* in [2].

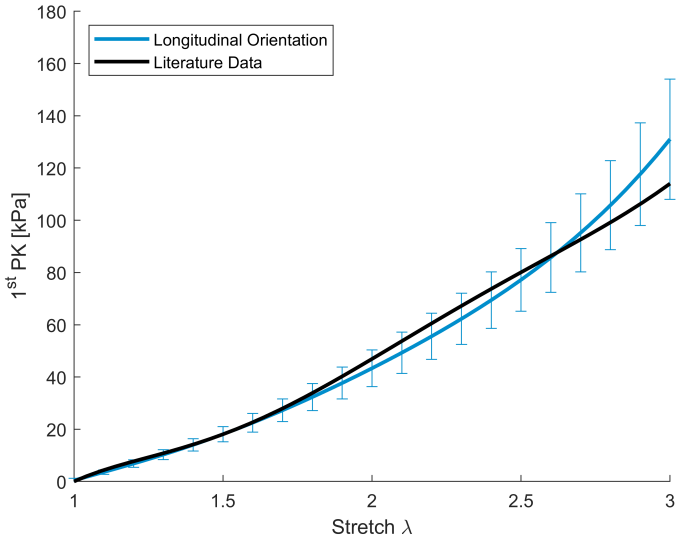

Figure 5.4: Direct comparison between obtained and published results.

The similarity from the results between the conducted tests during this work and the published results from Maryam Sami Jokandan *et al.* in [2], validate, by comparison, the experimental tests procedures.

5.4 Data Fitting

The next phase of the carried out work was to fit the proposed model from equation 4.20 with the data from the experimental results, figure 5.3d. As the uniaxial tests assess circular or longitudinal orientations to fit the uniaxial data, the proposed model only account for one family of fibres (similar to what was done in section 4.3.1).

The procedure to fit the proposed model to the uniaxial data was the same as explained in 4.3.1.1 when it was fitted to the published data in [2]. Figure 5.5 presents the results.

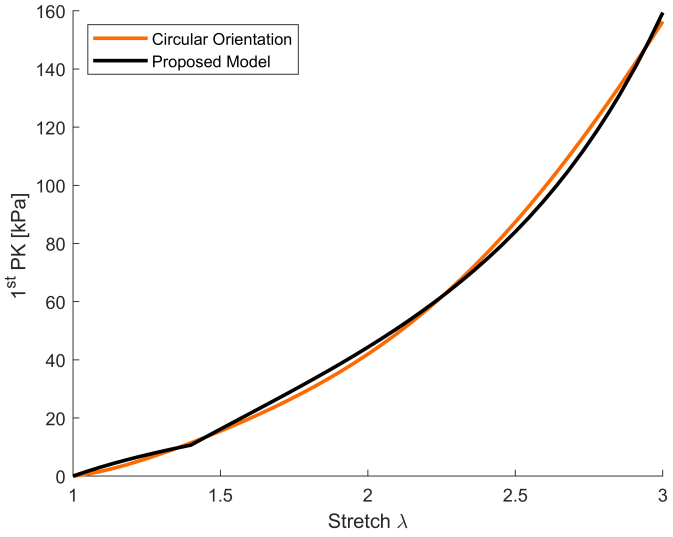

(a) Circular Orientation, $\lambda_r = 1.4 | C_{10} = 6\,\text{kPa} | k_1 = 68\,\text{kPa} | k_2 = 0.62$.

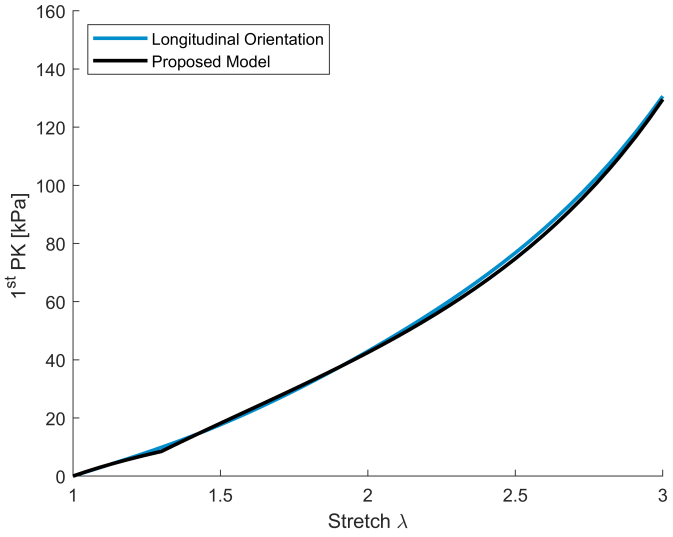

(b) Longitudinal Orientation $\lambda_r = 1.3 | C_{10} = 6\,\text{kPa} | k_1 = 46\,\text{kPa} | k_2 = 0.42$.

Figure 5.5: Experimental results fitted with proposed model.

5.5 Discussion

In the present uniaxial tests it was evaluated the response of the bladder wall tissue considering the two dominant orientations, longitudinal and circular respectively. There are some considerations to account for regarding the tests conducted during this work.

First, the origin of the bladder. It was used a bladder from a female porcine, ideally it would have been used a human bladder for a more beneficial characterization of the tissue, as there are some differences between the organs. Anatomically, the human bladder is an extraperitoneal organ when empty, while the porcine bladder is an intraperitoneal organ. S. E. Dahms *et al.* in [37] compared the ultimate tensile strength and stretch of human and porcine bladder. The results showed a similar ultimate tensile strength, $270 \pm 0.14\,\text{kPa}$ for the human bladder and $320 \pm 0.10\,\text{kPa}$. However, the ultimate tensile stretch of the human bladder is lower than the porcine bladder, respectably, 1.69 ± 0.17 compared with 2.66 ± 0.31, showing a lower compliance on the human bladder. Nevertheless, in the scope of this work, the characterization of the bladder to assess the applicability of the proposed pseudostrain-energy function is valid.

Second, the type of tests performed. As the bladder expands during filling, elongation of the bladder tissue occurs both in the longitudinal and circular direction. In order to compensate the difference in the real deformation gradient of the bladder whilst filling and the uniaxial deformation gradient, the samples were chosen in such a way that it made possible to assess the separate contribution of the longitudinal and circular orientations.

Finally, it is important to comment on the experimental conditions of the bladder. The bladder was collected and cleaned right after dissection and then frozen until the tests. According to the study of S. O'Leary *et al.* in [38] that analysed the impact of freezing on the mechanical properties of porcine aortic tissue and in general no significant difference was found in the mechanical properties of the tissue, therefore, it is assumed that the storage condition of the bladder is suitable. Another limitation of this study is using only using one bladder However, due to time and resources constraints it was only possible to test one bladder .

Regardless of the limitations of this study, the data was validated by comparison with previously published data and the proposed pseudostrain-energy function proved to fit the experimental results.

Chapter 6

Filling Simulation

6.1 Bladder Model

The final stage of this work was to perform an inflation simulation of the bladder. It was used a model of the bladder and urethra based on magnetic resonance imaging data of a nulliparous 24-year old female without pelvic floor dysfunction complaints developed by D. Oliveira *et al.* [39], figure 6.1. Recall figure 2.2, it is possible to identify within the model different parts of the bladder, figure 6.2. The simulation was performed using ABAQUS®.

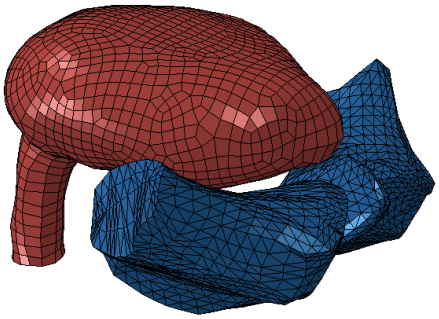

Figure 6.1: Model of the bladder, urethra and symphysis pubis [39].

ABAQUS® is a finite element analyses software capable of preprocessing, monitoring and postprocessing a problem. ABAQUS® has a wide range of material models. However, in the context of these work, proposing a new material model, it is necessary to apply a user-defined material. This can be done by a subroutine, developed in FORTRAN language, where the constitutive equations of the material model are defined. This subroutine is designated as a UMAT [40]. The implementation of the proposed pseudostrain-energy function is based on an UMAT developed by J. Ferreira [41].

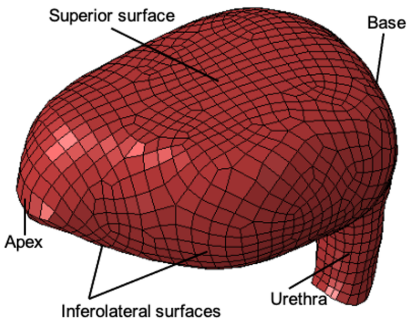

Figure 6.2: Superolateral view of the bladder - model.

Accordingly, there was a need to define the new material model, equation 4.20, within the UMAT. Once it was characterized, the UMAT was capable of enabling the use of a user-defined material based on equation 4.20, encompassing fibre recruitment and dispersion, following an angular integration approach. The subroutine script that implemented the angular integration approach can be found in appendix C.

6.2 Preferred Fibre Directions

The model is defined to consider two families of fibres, with longitudinal and circular orientations. To implement both families, it was needed to previously define the preferred fibre distribution within the bladder. Considering the problem as a heat transfer study, it is possible to determine an approximation of the orientation of the fibres combining the load, in the form of heat flux, and the boundary conditions (BC), in the form of a temperature. Longitudinal fibres are regarded as having an orientation from the apex to the base of bladder. Therefore, the combination of BC/Load needs to promote the path of the heat flux to follow the same orientation. Figure 6.3 shows the combinations used to determined the direction of circular and longitudinal fibres within the bladder wall. Following the results, figure 6.4, the preferred direction at the centroid of each element from the bladder wall is saved and then used in the simulation by the means of the UMAT.

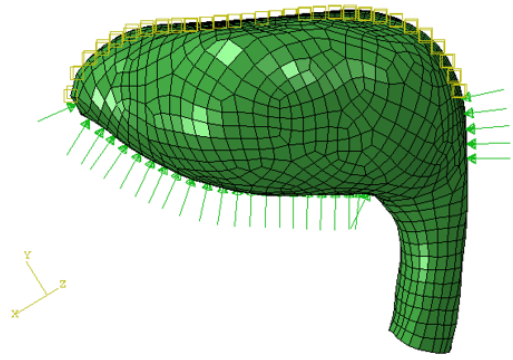

(a) Circular BC/Load set - Side View.

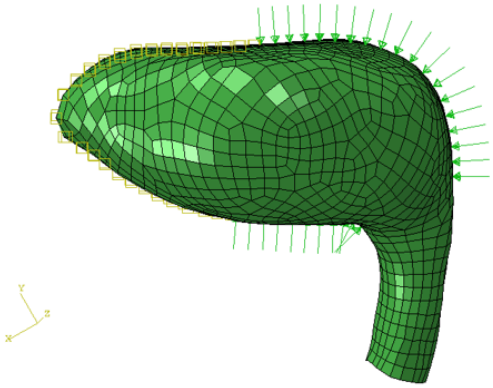

(b) Longitudinal BC/Load set - Side View.

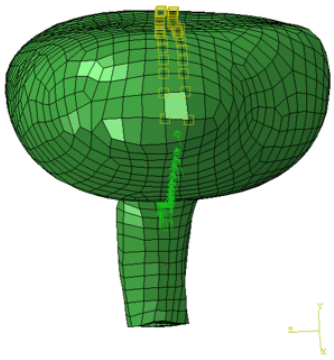

(c) Circular BC/Load set - Front View.

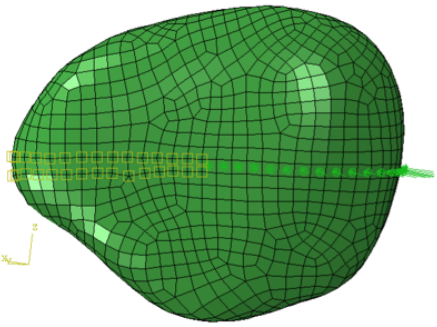

(d) Longitudinal BC/Load set - Top View.

Figure 6.3: BC/Load combinations.

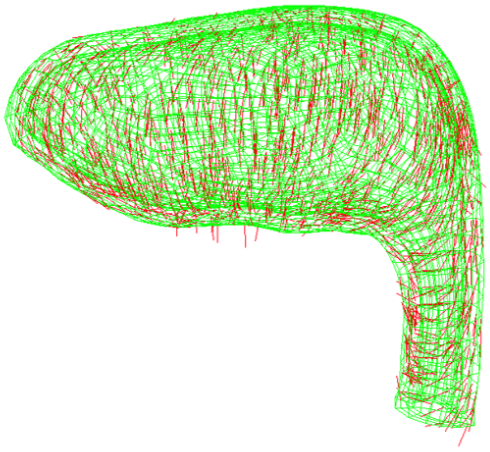

(a) Circular direction.

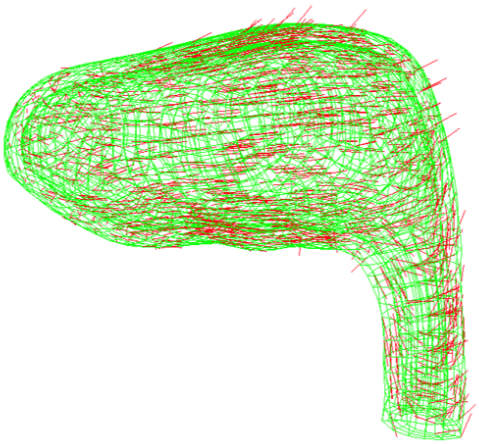

(b) Longitudinal direction.

Figure 6.4: Fibre preferred direction.

6.3 Load, Boundary Conditions and Material Properties

The new material model is defined within the UMAT with the parameter values obtained as best-fit from the experimental tests conducted, shown from figure 5.5,

- **Ground matrix:** $C_{10} = 6\,\text{kPa}$;
- **Circular fibre family:** $\lambda_\text{r} = 1.4 \mid k_1 = 68\,\text{kPa} \mid k_2 = 0.62$;
- **Longitudinal fibre family:** $\lambda_\text{r} = 1.3 \mid k_1 = 46\,\text{kPa} \mid k_2 = 0.62$.

The filling simulation is achieved through what is known as a surface-based fluid cavities simulation within the ABAQUS® software. Such simulations are used when there is a need to predict the mechanical response of a liquid-filled structure, in this case, the bladder. In this case, the liquid used was water. The maximum volume was imposed by the bladder model. Regarding boundary conditions of the conducted simulation, the end part of the urethra had a zero displacement boundary condition, and there was a possible general contact constraint between the bladder and the symphysis pubis bone, that used the penalty method to enforce the contact constrain.

6.4 Results and Discussion

As the new material model is defined within the UMAT, the simulation of the bladder filling was ready to be performed. Figure 6.5 and 6.6 shows the behaviour and geometrical changes of the bladder, while filling, at different volumes with the respective pressure. Each of the bladder wall model is representative of a layer (with exception of the adventitia layer which the mechanical contribution of this layer to the bladder wall properties is almost negligible [9]).

The pseudostrain-energy function on which the proposed model is based, was defined considering the microstructure of the bladder wall. The parameters and properties of the bladder on which the constitutive equation was based, were determined following the uniaxial data from the conducted experimental results. The model was then extrapolated to a bladder filling simulation, considering fibre dispersion. That being said, there is no direct way of comparing the results to verify the viability of the results from the simulation. However, the material model on which the simulation is based, have a direct influence on the pressure response of the bladder wall.

A. Parekh *et al.* in [42] studied the bladder filling in rats. Regarding the pressure [42] stated that the average peak pressure values was $2.23 \pm 0.19\,\text{kPa}$. The simulation conducted during this work, resulted in the pressure-volume curve in figure 6.7, showing a peak pressure of around 1.3 kPa. However, A. Parekh *et al.* in [42] studies were conducted on rats, while the simulations in the present work derive from porcine. S. E. Dahms *et al.* in [37] made a comparative analysis between rat, porcine and human bladder. He found

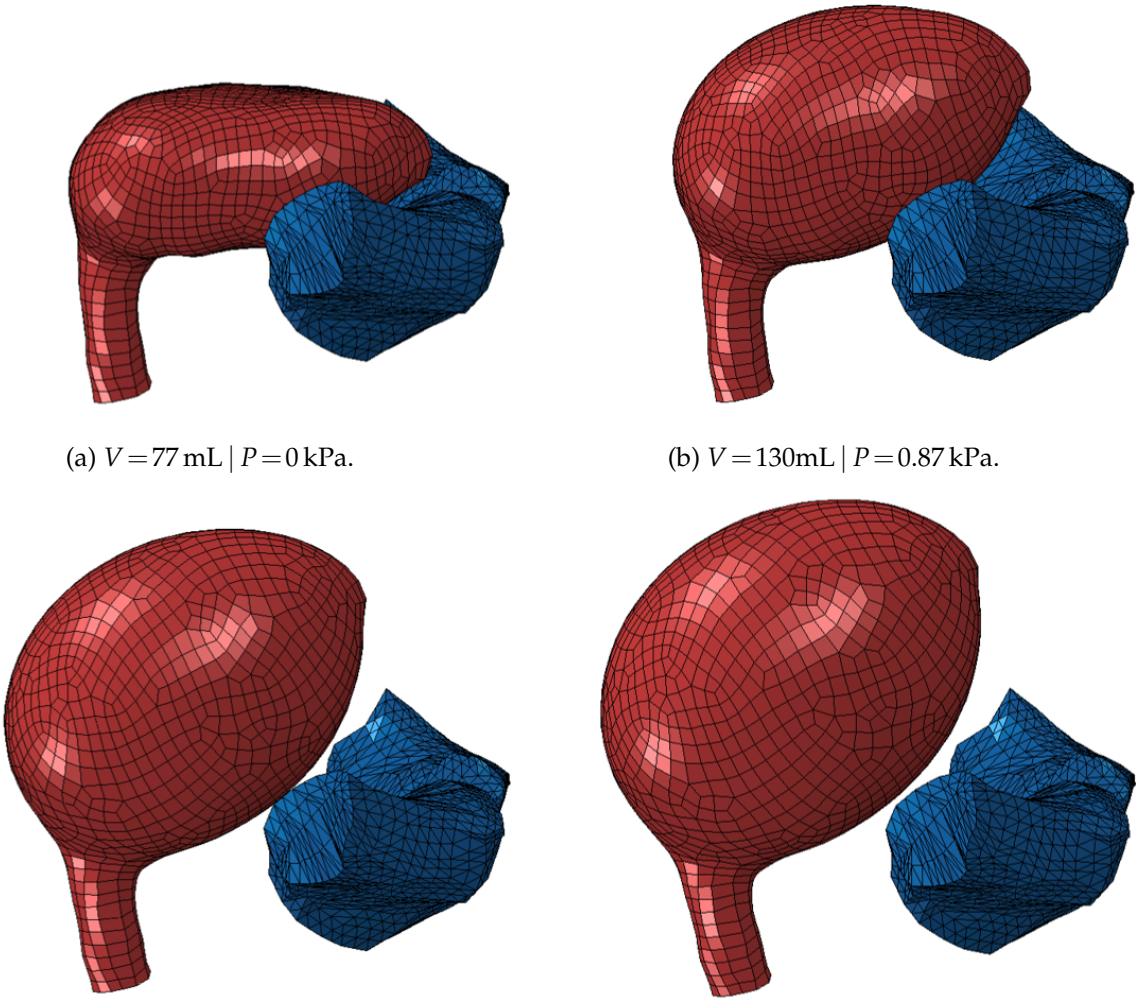

(a) $V = 77\,\text{mL} \mid P = 0\,\text{kPa}$. (b) $V = 130\text{mL} \mid P = 0.87\,\text{kPa}$.

(c) $V = 184\,\text{mL} \mid P = 1.17\,\text{kPa}$. (d) $V = 237\,\text{mL} \mid P = 1.27\,\text{kPa}$.

Figure 6.5: Bladder filling simulation.

out that the rat bladder, when compared to the porcine bladder, showed an increasement in stiffness of the bladder wall of around 2 times. Having this factor of 2 in consideration, the pressure response is within the expected range, by comparison.

Figure 6.7 apart from the pressure-volume curve, also shows the corresponding micturition phase. As the pressure reaches the plateau of the curve (peak pressure), the sensation of voiding starts to appear, characteristic of the voiding phase.

Finally, figure 6.8 shows the Cauchy stress - stretch curve. Also present in the figure is the fibre recruitment stretch of longitudinal and circular family of fibres. It is possible to observe a slope change in the curve within the recruitment stretch values of each recruitment fibre, implying the model correct assessment of fibre recruitment.

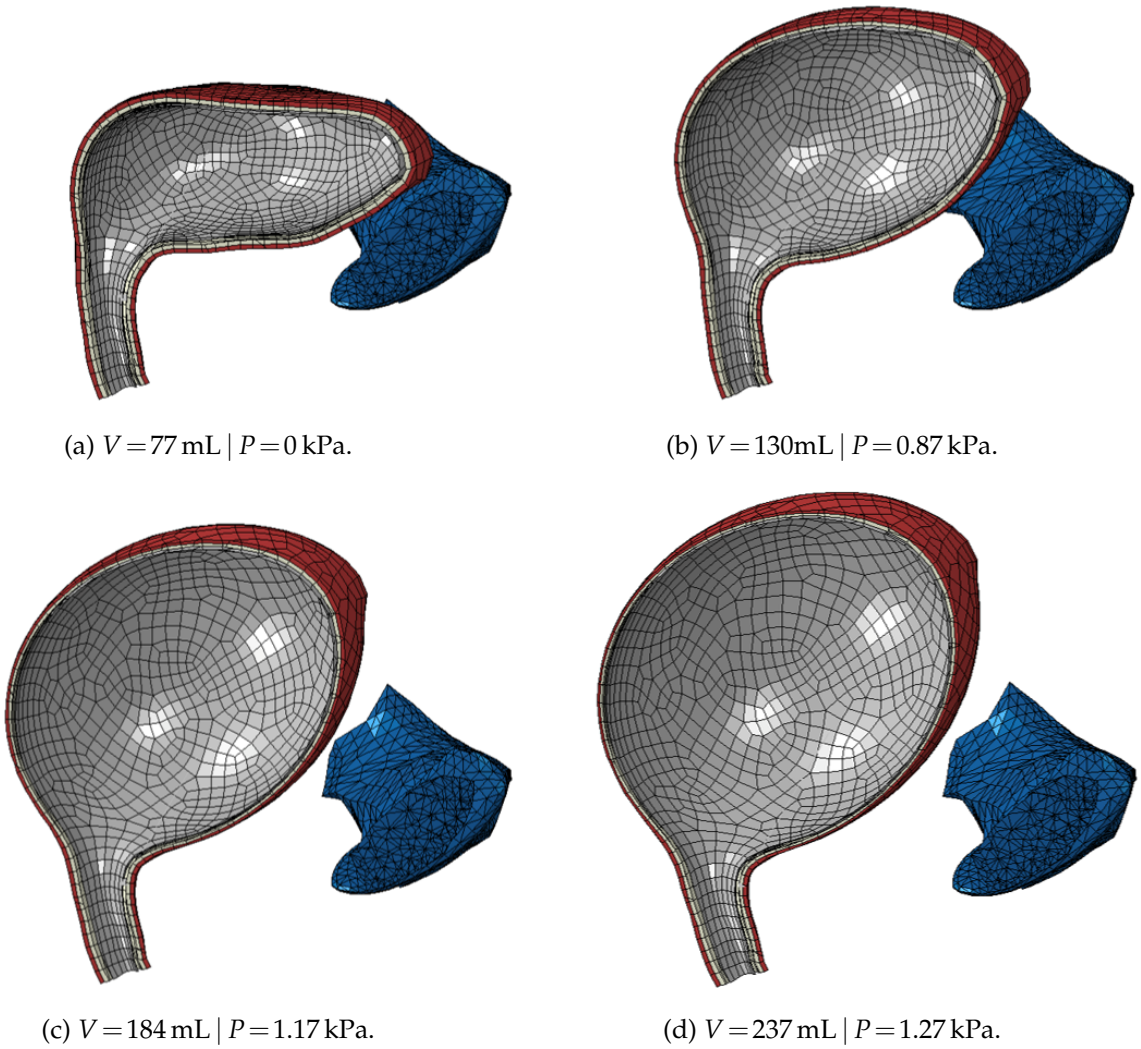

(a) $V = 77\,\text{mL} \mid P = 0\,\text{kPa}$.

(b) $V = 130\text{mL} \mid P = 0.87\,\text{kPa}$.

(c) $V = 184\,\text{mL} \mid P = 1.17\,\text{kPa}$.

(d) $V = 237\,\text{mL} \mid P = 1.27\,\text{kPa}$.

Figure 6.6: Bladder filling simulation - Cut view.

Fibre dispersion within the simulation was considered by the discretization method shown in equation 3.85, and the probability density function defined by the von Mises distribution, given by equation 4.21. Given the lack of data regarding the value of the concentration parameter b for the bladder wall, it was chosen a value, $b = 3$, which could provide good results and enable the verification of the UMAT assessment of fibre dispersion. To do so, a second simulation where no dispersion was considered. No dispersion was defined by a high value of b, $b = 30$. Figure 6.9 shows a direct comparison between the Cauchy stress response as a function of stretch for both simulations. Some observations can be made. The fibre recruitment happens at a slightly higher value of stretch when no dispersion is considered, this could be a resultant of the deformation gradient on the element in study. As the fibre recruitment is higher, the contribution of the fibres

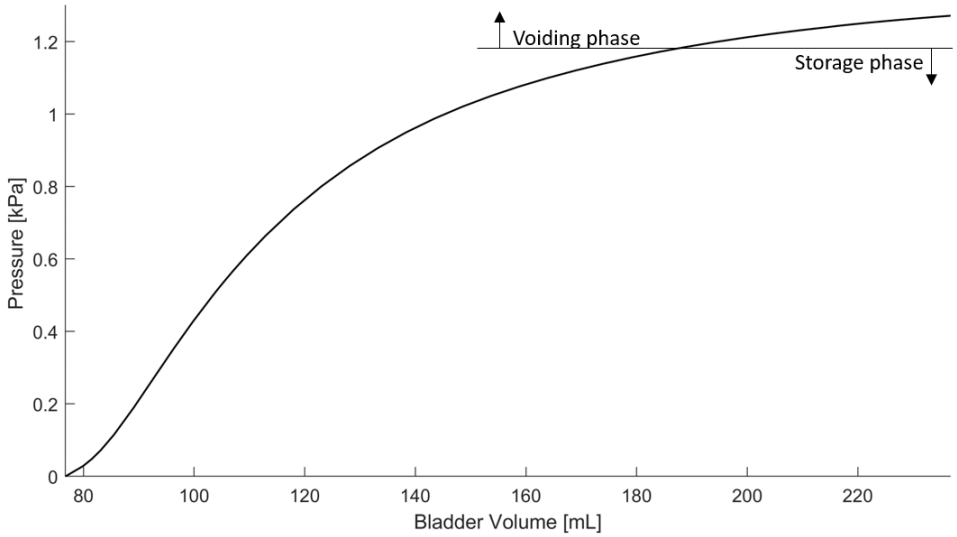

Figure 6.7: Pressure as a function of volume and respective micturition phase.

has a later start, hence the lower stress in the region of the recruitment stretch. However, a careful analysis shows the slope of the curve where no dispersion is considered higher, that can be translated to a stiffer model, expected when no dispersion is considered. This second simulation result analysis suggested that the fibre dispersion was being correctly implemented within the UMAT.

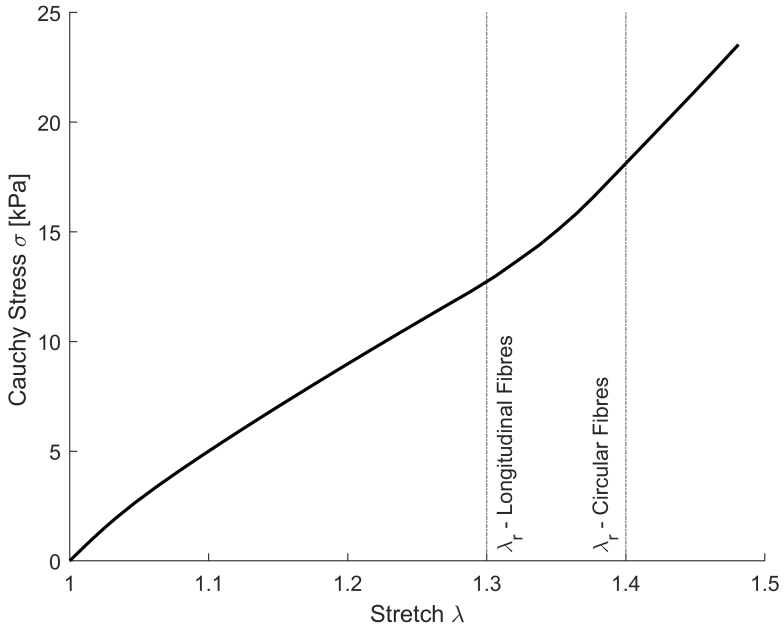

Figure 6.8: Cauchy stress response as a function of stretch and respective fibre recruitment range.

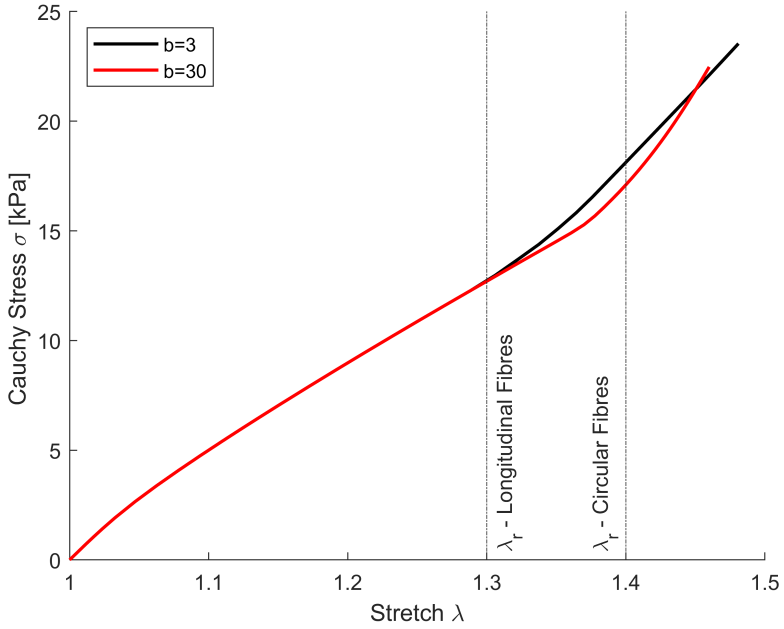

Figure 6.9: Cauchy stress response as a function of stretch and respective fibre recruitment range. Comparison between $b = 3$ and $b = 30$, representative of when dispersion is considered or not, respectively.

Chapter 7

Conclusions and Future Work

7.1 Conclusions

In this work a new pseudostrain-energy function Ψ of the bladder wall was proposed. The motivation of the form of the proposed function is derived from the microstructure of the bladder, considering both fibre recruitment and fibre dispersion. Fibre dispersion was considered introducing a material parameter for stretch recruitment, while fibre dispersion was considered following an angular integration approach. The material parameters have either a microstructural or phenomenological nature, implying the usage of image methods or mechanical tests, respectively.

The applicability of the proposed model was studied at first stage by curve fitting literature data of bladder testing. Then, uniaxial tests of a bladder from a female porcine were conducted. The sample layout within the bladder tissue allowed an assessment of differences between the two dominant fibre orientations of the bladder, longitudinal and circular, respectively. The experimental results allowed the proposed model to be defined as a contribution of a ground matrix, Ψ_{mat}, and two fibre families, $\Psi_{\text{fib}_{1,2}}$, each with a distinctive orientation.

The second and last phase of this work was to implement the new proposed model in an ABAQUS® simulation using a user-defined material known as an UMAT. Using a model obtained from magnetic resonance imaging data, the bladder behaviour was studied during filling. The performed simulation results, validated by the pressure behaviour in function of the bladder internal volume, showed the applicability of the proposed model, based on a microstructural approach, to a macroscale application, as the whole bladder was simulated. The shape of stress - stretch curve show the fibre recruitment, as observed by higher slopes at stretches greater than the recruitment, suggesting an accurate implementation of the fibre recruitment within the UMAT. A second performed simulation where no dispersion was considered, also implied the correct assessment of

fibre dispersion, as the slope of stress-stretch curve when no dispersion is considered is greater when compared to the situation when dispersion is considered.

The development of this work showed the proposed pseudostrain-energy function ability to characterize the bladder. This high ability to stretch was due to the inclusion of both fibre recruitment and dispersion. The implementation of the proposed model within an ABAQUS® model resulted in a capable simulation of the bladder filling in which fibre recruitment and fibre dispersion were considered. The parameters on which the bladder material is defined can be easily adjusted to fit curves of similar nature.

7.2 Future Work

For future works it would be important to determine the probability density function by imaging analyses of second harmonic generation, as it would provide a better approach to define the fibre dispersion within the bladder microstructure.

Conducting experimental tests on more specimens, preferentially on human bladders, would result in an improved characterization of the parameters on which the proposed model is based. Biaxial testing would also provide a better approximation of the bladder deformation state during filling.

A more complex bladder simulation model, obtained from magnetic resonance imaging, could result in a more realistic simulation, as the boundary conditions were adjusted to account for the interaction with surrounding organs and tissues.

As far as the simulation is concerned, it would be important to analyse the effects on the mechanical response as the bladder fills in unhealthy bladders, such as the ones having tumours or other urological dysfunctions.

Appendix A

Pseudostrain-energy function derivatives

Consider the new proposed model, defined in equation 4.20, can be rewritten as:

$$\begin{aligned}\Psi &= \Psi_{\text{mat}} + \Psi_{\text{fib}} \\ &= \mathrm{C}_{10}\left(\mathrm{I}_1 - 3\right) + \frac{1}{4\pi}\sum_{i=1}^{2}\int_{\mathbb{S}^2} f_i \rho_i(\mathbf{N})\,\frac{k_{1_i}}{2k_{2_i}}\left[e^{k_{2_i}\left(\sqrt{\mathrm{I}_{4\mathrm{n_i}}}-1\right)^2}-1\right]\mathrm{d}\mathbb{S}^2 \quad \text{with} \quad f_i = \begin{cases}1 & \lambda_{\mathrm{f}_i} > \lambda_{\mathrm{r}_i} \\ 0 & otherwise\end{cases}\end{aligned} \tag{A.1}$$

where,

$$W_i\left(\mathrm{I}_{4\mathrm{n_i}}\right) = \frac{k_{1_i}}{2k_{2_i}}\left[e^{k_{2_i}\left(\sqrt{\mathrm{I}_{4\mathrm{n_i}}}-1\right)^2}-1\right] \tag{A.2}$$

The Cauchy stress tensor $\boldsymbol{\sigma}$, can be defined as:

$$\boldsymbol{\sigma} = \boldsymbol{\sigma}_{\text{mat}} + \boldsymbol{\sigma}_{\text{fib}} - p\mathbf{I} \tag{A.3}$$

where, $\boldsymbol{\sigma}_{\text{mat}}$ is given by,

$$\boldsymbol{\sigma}_{\text{mat}} = 2J^{-1}\mathrm{C}_{10}\mathbf{b} \tag{A.4}$$

and, $\boldsymbol{\sigma}_{\text{fib}}$ is given as,

$$\boldsymbol{\sigma}_{\text{fib}} = f\frac{1}{2\pi}\sum_{i=1}^{2}\int_{\mathbb{S}^2}\rho_i(\mathbf{N})\,W_i^{'}\left(\mathrm{I}_{4\mathrm{n_i}}\right)\mathbf{n}\otimes\mathbf{n}\mathrm{d}\mathbb{S}^2 \tag{A.5}$$

where $\mathbf{n} = \mathbf{FN}$, and $W_i^{'}\left(\mathrm{I}_{4\mathrm{n_i}}\right)$ is the first derivative of $W_i\left(\mathrm{I}_{4\mathrm{n_i}}\right)$ in terms of $\mathrm{I}_{4\mathrm{n_i}}$, which is equal to:

$$W_i^{'}\left(\mathrm{I}_{4\mathrm{n_i}}\right) = \frac{k_{1_i}\left(\sqrt{\mathrm{I}_{4\mathrm{n_i}}}-1\right)e^{k_{2_i}\left(\sqrt{\mathrm{I}_{4\mathrm{n_i}}}-1\right)^2}}{2\sqrt{\mathrm{I}_{4\mathrm{n_i}}}} \tag{A.6}$$

Other stress tensors can be defined in relation to the Cauchy stress tensor $\boldsymbol{\sigma}$.

The second derivative of $W_i\left(\mathrm{I}_{4\mathrm{n_i}}\right)$ can be written as,

$$W_i^{''}\left(\mathrm{I}_{4\mathrm{n_i}}\right) = \frac{k_{1_i} k_{2_i}\left(\sqrt{\mathrm{I}_{4\mathrm{n_i}}}-1\right)^2 e^{k_{2_i}\left(\sqrt{\mathrm{I}_{4\mathrm{n_i}}}-1\right)^2}}{2\mathrm{I}_{4\mathrm{n_i}}} + \frac{k_{1_i} e^{k_{2_i}\left(\sqrt{\mathrm{I}_{4\mathrm{n_i}}}-1\right)^2}}{4\mathrm{I}_{4\mathrm{n_i}}} - \frac{k_{1_i}\left(\sqrt{\mathrm{I}_{4\mathrm{n_i}}}-1\right) e^{k_{2_i}\left(\sqrt{\mathrm{I}_{4\mathrm{n_i}}}-1\right)^2}}{4{\mathrm{I}_{4\mathrm{n_i}}}^{3/2}} \tag{A.7}$$

Appendix B

MATLAB Script

```
clear all
clc
syms t l p_0 p_1 p_2 x
syms C11 C12 C13 C21 C22 C23 C31 C32 C33 ;

C_symb=[C11 C12 C13;
        C21 C22 C23;
        C31 C32 C33];

I1=trace(C_symb);
J_symb=sqrt(det(C_symb));

t=0; %fibre preferred angle
N=[cos(t);sin(t);0];

%Model Parameters
lr=1.0; %recruitment stretch
C10=1.0;
k1=1.0;
k2=1.0;

lambdaf=sqrt(N'*C_symb*N);
I4=(lambdaf/lr)^2;

%Proposed pseudostrain-energy function
    Y_m=C10*(I1-3);
    Y_f=piecewise(lambdaf<lr, 0,lambdaf>=lr,k1*(exp(k2*(sqrt(I4)-1)^2)-1)/(2*k2));
    Y=Y_m+Y_f-p_1*(J_symb-1);

    S_symb=2*[diff(Y,C11) diff(Y,C12) diff(Y,C13);
              diff(Y,C21) diff(Y,C22) diff(Y,C23);
              diff(Y,C31) diff(Y,C32) diff(Y,C33)];

```

```
34
35 % Deformation Gradient
36
37 test='uni'; %'uni' \\ 'bi' \\ 'shear'
38 switch test
39     case 'uni'
40         F=[l 0 0;0 1/sqrt(l) 0;0 0 1/sqrt(l)];
41     case 'bi'
42         F=[l 0 0; 0 l 0; 0 0 1/(l^2)];
43 end
44
45
46 C=F'*F;
47
48 %2nd PK stress tensor
49 S=subs(S_symb,C_symb,C);
50
51 %Jacobian
52 J=subs(J_symb,C_symb,C);
53
54
55 sigma=(1/J)*F*S*F';
56
57
58 % Boundary Condition
59 p_f=solve(sigma(3,3)==0,p_1);
60
61
62 sigma_f=subs(sigma,p_1,p_f);
63
64 %1st PK stress tensor
65 pkk_=J*F^-1*sigma_f;
66
67
68 % (1,1) components of stress tensors
69 S_xx=sigma_f(1,1);
70 pkk_xx=pkk_(1,1);
71
72 %1st PK stress tensor plot
73 figure(1)
74 hold on
75 xlabel('Stretch \lambda');
76 ylabel('1^{st} PK');
77 fplot(pkk_xx,[1 3],'k')
```

Appendix C

Angular Integration Subroutine

```
1
2  SUBROUTINE anisomat_discrete(cmname,w,sfic,cfic,f,props,  &
3      efi,noel,npt,kinc,det,factor,ndi)
4
5  !>    AFFINE NETWORK: 'FICTICIOUS' CAUCHY STRESS AND ELASTICITY
       TENSOR
6  !> DISCRETE ANGULAR INTEGRATION SCHEME (icosahedron)
7  use global
8  IMPLICIT NONE
9
10 INTEGER, INTENT(IN)                          :: ndi
11 DOUBLE PRECISION, INTENT(OUT)                :: sfic(ndi,ndi)
12 DOUBLE PRECISION, INTENT(OUT)                :: cfic(ndi,ndi,ndi,ndi)
13 DOUBLE PRECISION, INTENT(IN OUT)             :: f(ndi,ndi)
14 DOUBLE PRECISION, INTENT(IN)                 :: props(7)
15 DOUBLE PRECISION, INTENT(IN OUT)             :: efi
16 INTEGER, INTENT(IN OUT)                      :: noel,npt, kinc
17 DOUBLE PRECISION, INTENT(IN OUT)             :: det
18 CHARACTER (LEN=8), INTENT(IN OUT)            :: cmname
19
20 INTEGER :: j1,k1,l1,m1
21 DOUBLE PRECISION :: sfibfic(ndi,ndi), cfibfic(ndi,ndi,ndi,ndi),
22 DOUBLE PRECISION :: mfi(ndi),mf0i(ndi)
23 DOUBLE PRECISION :: aux,lambdai,dwi,ddwi,ddwi1,ddwi2,ddwi3
24 DOUBLE PRECISION :: bdisp,ang,w,wi,rho,aux2
25 DOUBLE PRECISION :: avga,maxa,suma,dirmax(ndi),kk1,kk2,ei
26
```

```
! INTEGRATION SCHEME
integer ( kind = 4 ) node_num
integer ( kind = 4 ) a
real ( kind = 8 ) a_xyz(3)
real ( kind = 8 ) a2_xyz(3)
real ( kind = 8 ) ai !area of triangle i
real ( kind = 8 ) area_total
integer ( kind = 4 ) b
real ( kind = 8 ) b_xyz(3)
real ( kind = 8 ) b2_xyz(3)
integer ( kind = 4 ) c
real ( kind = 8 ) c_xyz(3)
real ( kind = 8 ) c2_xyz(3)
integer ( kind = 4 ) edge_num
integer ( kind = 4 ), allocatable, dimension ( :, : ) :: edge_point
integer ( kind = 4 ) f1
integer ( kind = 4 ) f2
integer ( kind = 4 ) f3
integer ( kind = 4 ) face
integer ( kind = 4 ) face_num
integer ( kind = 4 ), allocatable, dimension ( : ) :: face_order
integer ( kind = 4 ), allocatable, dimension ( :, : ) :: face_point
integer ( kind = 4 ) face_order_max
integer ( kind = 4 ) factor
real ( kind = 8 ) node_xyz(3)
real ( kind = 8 ), parameter :: pi = 3.141592653589793D+00
real ( kind = 8 ), allocatable, dimension ( :, : ) :: point_coord
integer ( kind = 4 ) point_num
real ( kind = 8 ) rr, aa
real ( kind = 8 ) v

!  Size the icosahedron.
!
call icos_size ( point_num, edge_num, face_num, face_order_max )
!
!  Set the icosahedron.
!
allocate ( point_coord(1:3,1:point_num) )
allocate ( edge_point(1:2,1:edge_num) )
allocate ( face_order(1:face_num) )
```

```
67  allocate ( face_point(1:face_order_max,1:face_num) )
68
69  call icos_shape ( point_num, edge_num, face_num, face_order_max, &
70  point_coord, edge_point, face_order, face_point )
71  !
72  !  Initialize the integral data.
73  !
74  rr = 0.0D+00
75  area_total = 0.0D+00
76  node_num = 0
77
78  !! initialize the model data
79  !     fibers
80  kk1       = props(4)
81  kk2       = props(5)
82  bdisp     = props(6)
83  lr        = props(7)
84
85  aux=two*(det**(-one))
86  aux2=four*(det**(-four/three))
87  cfic=zero
88  sfic=zero
89
90  aa = zero
91  rr = zero
92  avga=zero
93  maxa=zero
94  suma=zero
95  dirmax=zero
96
97  !  Pick a face of the icosahedron, and identify its vertices as A, B
       , C.
98  !
99  do face = 1, face_num
100 !
101 a = face_point(1,face)
102 b = face_point(2,face)
103 c = face_point(3,face)
104 !
105 a_xyz(1:3) = point_coord(1:3,a)
```

```
106 b_xyz(1:3) = point_coord(1:3,b)
107 c_xyz(1:3) = point_coord(1:3,c)
108 !
109 !  Some subtriangles will have the same direction as the face.
110 !  Generate each in turn, by determining the barycentric coordinates
111 !  of the centroid (F1,F2,F3), from which we can also work out the
    barycentric
112 !  coordinates of the vertices of the subtriangle.
113 !
114 do f3 = 1, 3 * factor - 2, 3
115   do f2 = 1, 3 * factor - f3 - 1, 3
116
117     f1 = 3 * factor - f3 - f2
118
119     call sphere01_triangle_project ( a_xyz, b_xyz, c_xyz, f1, f2, f3
        , &
120       node_xyz )
121       ! From "Quadrature on the Surface of the Unit Sphere"
          available at https://people.sc.fsu.edu/~jburkardt/f_src/
          sphere_quad/sphere_quad.html
122     call sphere01_triangle_project ( &
123       a_xyz, b_xyz, c_xyz, f1 + 2, f2 - 1, f3 - 1, a2_xyz )
124     call sphere01_triangle_project ( &
125       a_xyz, b_xyz, c_xyz, f1 - 1, f2 + 2, f3 - 1, b2_xyz )
126     call sphere01_triangle_project ( &
127       a_xyz, b_xyz, c_xyz, f1 - 1, f2 - 1, f3 + 2, c2_xyz )
128
129     call sphere01_triangle_vertices_to_area ( a2_xyz, b2_xyz, c2_xyz
        , ai )
130
131     !direction of the sphere triangle barycenter - direction i
132     mf0i=node_xyz
133     CALL deffib(lambdai,mfi,mf0i,f,ndi) ! fibre stretch
134
135     CALL bangle(ang,f,mfi,noel,ndi,cmname) !fibre angle with
        preferred direction
136     CALL density(rho,ang,bdisp,efi)
137     !scaled weight
138     ai = ai/(two*pi)
139     !strain-like of fiber i
```

```
140
141
142     lambdai=lambdai/lr !normalized stretch
143     ei = lambdai-one
144      !calculate fiber sef and sef derivatives values
145     if (ei .ge. zero) then
146       !fiber sef
147       wi    = (kk1/(two*kk2))*(dexp(kk2*ei*ei)-one)
148       !1st & 2nd derivatives
149       dwi=(kk1/(two*sqrt(lambdai)))*((sqrt(lambdai)-one)*(dexp(kk2*(
              sqrt(lambdai)-one)*(sqrt(lambdai)-one))))
150       ddwi1=(kk1*kk2*(sqrt(lambdai)-one)*(sqrt(lambdai)-one)*(dexp(
              kk2*(sqrt(lambdai)-one)*(sqrt(lambdai)-one))))/(two*lambdai
              )
151       ddwi2=(kk1*(dexp(kk2*(sqrt(lambdai)-one)*(sqrt(lambdai)-one)))
              )/(four*lambdai)
152       ddwi3=(-kk1*(sqrt(lambdai)-one)*(dexp(kk2*(sqrt(lambdai)-one)
              *(sqrt(lambdai)-one))))/(four*(lambdai**(three/two)))
153       ddwi=ddwi1+ddwi2+ddwi3
154       !stress and material tangent
155     CALL sigfibfic(sfibfic,rho,dwi,mfi,ai,ndi) ! Cauchy Stress
156     !
157     CALL csfibfic(cfibfic,rho,dwi,ddwi,mfi,ai,ndi) !Tangent Matrix
158 !
159     DO j1=1,ndi
160        DO k1=1,ndi
161           sfic(j1,k1)=sfic(j1,k1)+aux*sfibfic(j1,k1)
162           DO l1=1,ndi
163             DO m1=1,ndi
164               cfic(j1,k1,l1,m1)=cfic(j1,k1,l1,m1)+aux2*cfibfic(j1,k1
                      ,l1,m1)
165             END DO
166           END DO
167        END DO
168      END DO
169 !
170     w=w+rho*ai*wi
171     aa=aa+1
172    endif
173     rr = rr +  rho*ai
```

```
174     node_num = node_num + 1
175     area_total = area_total + ai
176   end do
177 end do
178 f1 + 1, f2 - 2, f3 + 1, b2_xyz )
179 end do
180
181 deallocate ( edge_point )
182 deallocate ( face_order )
183 deallocate ( face_point )
184 deallocate ( point_coord )
185
186 RETURN
187 END SUBROUTINE anisomat_discrete
```

References

[1] Richard L. Drake, A. Wayne Vogl, and Adam W.M. Mitchell. Elsevier, 2020.

[2] Maryam Jokandan, Fatemeh Ajalloueian, Magnus Edinger, Peter Stubbe, Stefania Baldursdottir, and Ioannis Chronakis. Bladder wall biomechanics: A comprehensive study on fresh porcine urinary bladder. *Journal of the Mechanical Behavior of Biomedical Materials*, 79, 11 2017.

[3] Sara Roccabianca and Tamara Bush. Understanding the mechanics of the bladder through experiments and theoretical models: Where we started and where we are heading. *TECHNOLOGY*, 04:1–12, 03 2016.

[4] Anand K. Pater and Christopher R. Chapple. Anatomy of the lower urinary tract. *Surgery (Oxford)*, 26, 4 2008.

[5] National Institute of Diabetes, Digestive, and Kidney Diseases. The urinary tract how it works, availabe at: `https://www.niddk.nih.gov/health-information/urologic-diseases/urinary-tract-how-it-works`, 18/06/2021, 2020.

[6] Duane Hickling, Tung-Tien Sun, and Xue-Ru Wu. Anatomy and physiology of the urinary tract: Relation to host defense and microbial infection. *Microbiology spectrum*, 3, 09 2015.

[7] Fatemeh Ajalloueian, Greg Lemon, Joens Hilborn, Ioannis Chronakis, and Magdalena Fossum. Bladder biomechanics and the use of scaffolds for regenerative medicine in the urinary bladder. *Nature Reviews Urology*, 15, 02 2018.

[8] National Cancer Institute. Urinary bladder, available at `https://training.seer.cancer.gov/anatomy/urinary/components/bladder.html`, 18/06/2021.

[9] W. Artibani C.G. Fontanella E.L. Carniel E.M. Zanetti A.N. Natali, A.L. Audenino. Bladder tissue biomechanical behavior: Experimental tests and constitutive formulation. *Journal of Biomechanics*, 48, 2015.

[10] Oliver Hakenberg, Clemens Linne, Andreas Manseck, and Manfred Wirth. Bladder wall thickness in normal adults and men with mild urinary tract symptoms and benign prostatic enlargement. *Neurourology and urodynamics*, 19:585–93, 02 2000.

[11] Martin Kaefer, David Zurakowski, Stuart Bauer, Alan Retik, Craig Peters, Anthony Atala, and S. Treves. Estimating normal bladder capacity in children. *The Journal of urology*, 158:2261–4, 12 1997.

[12] L. Brubaker M.P. FitzGerald, U. Stablein. Urinary habits among asymptomatic women. *American Journal of Obstetric & Gynecology*, 187, 11 2002.

[13] E Lukacz, C Sampselle, M Gray, S Macdiarmid, M Rosenberg, Pamela Ellsworth, and Mary Palmer. A healthy bladder: A consensus statement. *International journal of clinical practice*, 65:1026–36, 10 2011.

[14] Virginia Monteiro. *Computational Model of the Human Urinary Bladder*. PhD thesis, 06 2013.

[15] National Institute of Diabetes, Digestive, and Kidney Diseases. Bladder diseases, available at `https://medlineplus.gov/bladderdiseases.html`, 19-06-2021.

[16] Malgorzata Lekka, Piotr Laidler, Gil Dorota, Janusz Lekki, Zbigniew Stachura, and AZ Hrynkiewicz. Lekka, m, laidler, p, gil, d, lekki, j, stachura, z and hrynkiewicz, az. elasticity of normal and cancerous human bladder cells studied by scanning force microscopy. eur biophys j 28: 312-316. *European biophysics journal : EBJ*, 28:312–6, 02 1999.

[17] Gabriel Lee and C.T. Lim. Biomechanics approaches to studying human diseases. *Trends in biotechnology*, 25:111–8, 04 2007.

[18] Eduardo W. Chaves. *Notes on Continuum Mechanics*. Springer, 01 2013.

[19] Gerhard Holzapfel. *Nonlinear solid mechanics: a continuum approach for engineering*. Wiley, 01 2000.

[20] Nam Kim. *Introduction to Nonlinear Finite Element Analysis*. Springer, 11 2014.

[21] Gerhard Holzapfel, Ray Ogden, and Selda Sherifova. On fibre dispersion modelling of soft biological tissues: A review. *Proceedings of the Royal Society A: Mathematical, Physical and Engineering Sciences*, 475:20180736, 04 2019.

[22] Thomas Gasser, Ray Ogden, and Gerhard Holzapfel. Hyperelastic modeling of arterial layers with distributed collagen fibre orientations. *Journal of the Royal Society, Interface / the Royal Society*, 3:15–35, 02 2006.

[23] Thomas Gasser, Ray Ogden, and Gerhard Holzapfel. Hyperelastic modeling of arterial layers with distributed collagen fibre orientations. *Journal of the Royal Society, Interface / the Royal Society*, 3:15–35, 02 2006.

[24] Gerhard Holzapfel and Ray Ogden. Constitutive modelling of arteries. *Proceedings of The Royal Society A Mathematical Physical and Engineering Sciences*, 466:1551–1597, 04 2010.

[25] Y. Lanir. Constitutive equations for fibrous connective tissues. *Journal of Biomechanics*, 16, 1983.

[26] Kewei Li, Ray Ogden, and Gerhard Holzapfel. A discrete fibre dispersion method for excluding fibres under compression in the modelling of fibrous tissues. *Journal of The Royal Society Interface*, 15:20170766, 01 2018.

[27] Fangzhou Cheng, Anne Robertson, Lori Birder, Aura Kullmann, Jack Hornsby, Paul Watton, and Simon Watkins. Layer dependent role of collagen recruitment during loading of the rat bladder wall. *Biomechanics and Modeling in Mechanobiology*, 17, 04 2018.

[28] Kewei Li and Gerhard Holzapfel. Multiscale modeling of fiber recruitment and damage with a discrete fiber dispersion method. *Journal of the Mechanics and Physics of Solids*, 126:226–244, 02 2019.

[29] Michael Hill, Xinjie Duan, Gregory Gibson, Simon Watkins, and Anne Robertson. A theoretical and non-destructive experimental approach for direct inclusion of measured collagen orientation and recruitment into mechanical models of the artery wall. *Journal of biomechanics*, 45:762–71, 03 2012.

[30] Pedro Martins, Renato Natal Jorge, and Antonio Ferreira. A comparative study of several material models for prediction of hyperelastic properties: Application to silicone-rubber and soft tissues. *Strain*, 42:135–147, 08 2006.

[31] R. W. Ogden. Large deformation isotropic elasticity: on the correlation of theory and experiment for compressible rubberlike solids. *Proceedings of the Royal Society of London. Series A, Mathematical and Physical Sciences*, 06 1972.

[32] Gerhard Holzapfel, Thomas Gasser, and Ray Ogden. A new constitutive framework for arterial wall mechanics and a comparative study of material models. *Journal of Elasticity*, 61:1–48, 04 2012.

[33] J. D. Humphrey and F. C. P. Yin. A new constitutive formulation for characterizing the mechanical behavior of soft tissues. *Biophysical Journal*, 52, 1987.

[34] Chew P. H. Yin, F. C. P. and S. L. Zeger. An approach to quantification of biaxial tissue stress-strain data. *Journal of Biomechanics*, 19, 1986.

[35] J. D. Humphrey and F. C. P. Yin. On constitutive relations and finite deformations of passive cardiac tissue: I. a pseudostrain-energy function. *Journal of Biomechanical Engineering*, 109, 11 1987.

[36] Pedro Martins, Agnaldo Silva-Filho, Andrea Fonseca, Agostinho Santos, Liliana Santos, Teresa Mascarenhas, Renato Natal Jorge, and Antonio Ferreira. Uniaxial mechanical behavior of the human female bladder. *International urogynecology journal*, 22:991–5, 04 2011.

[37] R. Dahiya T. F. Lue E. A. Tanagho S. E. Dahms, H. J. Piechota. Composition and biomechanical properties of the bladder acellular matrix graft: comparative analysis in rat, pig and human. *British Journal of Urology*, 09 1998.

[38] Siobhan O'Leary, Barry Doyle, and Tim Mcgloughlin. The impact of long term freezing on the mechanical properties of porcine aortic tissue. *Journal of the Mechanical Behavior of Biomedical Materials*, 37, 09 2014.

[39] D. Oliveira, M. Parente, and R. Jorge. Biocomputational model for urodynamics analysis. 2017.

[40] ABAQUS. Umat, available at `https://abaqus-docs.mit.edu/2017/English/SIMACAESUBRefMap/simasub-c-umat.htm#simasub-c-umat`, 10/06/2021.

[41] J. Ferreira. Umat - abaqus library, available at https://github.com/jpsferreira/UMAT-ABAQUS_library, 15/02/2021.

[42] S. Wognum R. L. Heise M. B. Chancellor M. S. Sacks A. Parekh, A. D. Cigan. Ex vivo deformations of the urinary bladder wall during whole bladder filling: Contributions of extracellular matrix and smooth muscle. *Journal of Biomechanics*, 02 2010.